T.C.
BOLU ABANT İZZET BAYSAL UNIVERSITY
INSTITUTE OF GRADUATE STUDIES
DEPARTMENT OF PHYSICS

SYNTHESIS OF MO- AND W- DOPED ZNO THIN FILMS VIA THE SOL-GEL TECHNIQUE: STRUCTURAL, OPTICAL, AND ELECTRICAL PROPERTIES

DOCTOR OF PHILOSOPHY, PHYSICS

SİNAN ÖZTEL

THESIS SUPERVISOR
PROF. DR. ALİEKBER AKTAĞ

BOLU, DECEMBER 2025

ACCEPTANCE AND APPROVAL PAGE

The thesis entitled "**SYNTHESIS OF MO- AND W- DOPED ZNO THIN FILMS VIA THE SOL-GEL TECHNIQUE: STRUCTURAL, OPTICAL, AND ELECTRICAL PROPERTIES"**, prepared by **Sinan ÖZTEL** has been approved by our jury with unanimity vote as a Doctoral Thesis in the Department of Physics, Program of Physics Ph.D December 29, 2025.

Jury Members	**Signature**
Supervisor Prof. Dr. Aliekber AKTAĞ Bolu Abant Izzet Baysal University	.....
Member Prof. Dr. Ercan YILMAZ Bolu Abant Izzet Baysal University	.....
Member Assoc. Prof. Dr. Erhan BUDAK Bolu Abant Izzet Baysal University	.....
Member Prof. Dr. Kadir GÖKŞEN Duzce University	.....
Member Prof. Dr. Haydar ARSLAN Zonguldak Bulent Ecevit University	.....

Approval of the Institute of Graduate Studies

Prof. Dr. İbrahim KÜRTÜL

Director, Institute of Graduate Studies

ETHICAL STATEMENT

In this thesis, which I have prepared in accordance with the Thesis Writing Guide and Template of Bolu Abant İzzet Baysal University, Institute of Graduate Studies:

- I declare that the data, information, and documents presented in the thesis have been obtained in line with academic and ethical principles,
- That all information, documents, evaluations, and results are presented in accordance with the rules of scientific ethics and integrity,
- That I have properly cited and referenced all the works I benefited from in this thesis,
- That I have not made any alterations to the data used,
- And that the work presented in this thesis is original.

I also acknowledge that I accept all possible legal consequences and loss of rights that may arise otherwise.

According to the similarity report obtained through the Turnitin program, with filters determined by the Institute Directorate, the similarity index of the thesis does not exceed 30%.

.....

SİNAN ÖZTEL

ABSTRACT

SYNTHESIS OF MO- AND W- DOPED ZNO THIN FILMS VIA THE SOL-GEL TECHNIQUE: STRUCTURAL, OPTICAL, AND ELECTRICAL PROPERTIES
PHD THESIS
SİNAN ÖZTEL
BOLU ABANT İZZET BAYSAL UNIVERSITY
INSTITUTE OF GRADUATE STUDIES
DEPARTMENT OF PHYSICS
(SUPERVISOR: PROF. DR. ALİEKBER AKTAĞ)
BOLU, DECEMBER 2025
XIII + 69

In this study, molybdenum (2% and 4%) and tungsten (2%) doped zinc oxide (ZnO) thin films were synthesized via the sol–gel spin-coating technique to investigate the effects of high-valence dopants on the structural, vibrational, and electrical behavior of ZnO. The structural properties were examined using X-ray diffraction (XRD), while Fourier-transform infrared spectroscopy (FTIR) was utilized to identify Zn–O bonding characteristics and to evaluate the impact of dopant incorporation on vibrational modes. Spectral analyses were employed to determine the band gap variations, revealing that Mo and W dopants induced notable changes in lattice strain and electronic transitions. Electrical characterization using current–voltage (I–V) measurements showed that dopant concentration significantly affects carrier transport, ideality factor, and Schottky barrier parameters. Moreover, the quality of the diode structure was assessed based on the calculated ideality factors, providing insight into interfacial properties and transport mechanisms. Overall, the findings demonstrate that sol–gel-derived Mo- and W-doped ZnO thin films exhibit enhanced properties suitable for transparent electronics, diode applications, and advanced sensing technologies.

KEYWORDS: Thin Film, Zinc Oxide, Molybdenum, Tungsten

ÖZET

SOL-JEL TEKNİĞİ İLE MO- VE W- KATKILI ZNO İNCE FİLMLERİN SENTEZİ: YAPISAL, OPTİK VE ELEKTRİKSEL ÖZELLİKLERİ
DOKTORA TEZİ
SİNAN ÖZTEL
BOLU ABANT İZZET BAYSAL ÜNİVERSİTESİ
LİSANSÜSTÜ EĞİTİM ENSTİTÜSÜ
FİZİK ANA BİLİM DALI
(TEZ DANIŞMANI: PROF. DR. ALİEKBER AKTAĞ)
BOLU, ARALIK 2025
XIII + 69

Bu çalışmada, yüksek değerlikli katkılayıcıların ZnO'nun yapısal, titreşimsel ve elektriksel özellikleri üzerindeki etkilerini incelemek amacıyla molibden (%2 ve %4) ve tungsten (%2) katkılı çinko oksit (ZnO) ince filmler sol–jel döndürme kaplama yöntemi ile sentezlenmiştir. Filmlerin yapısal özellikleri X-ışını kırınımı (XRD) ile incelenmiş, katkı elementlerinin Zn–O bağlanma karakteristikleri ve titreşim modları üzerindeki etkilerini değerlendirmek amacıyla Fourier dönüşümlü kızılötesi spektroskopisi (FTIR) kullanılmıştır. Bant aralığı davranışları spektral analizler ile belirlenmiş ve Mo ile W katkılarının kafes gerilimi ile elektronik geçişlerde dikkate değer değişimlere yol açtığı görülmüştür. Akım–gerilim (I–V) ölçümlerine dayalı elektriksel karakterizasyon, katkı konsantrasyonunun taşıyıcı taşınımı, idealite faktörü ve Schottky bariyer parametreleri üzerinde belirgin bir etkiye sahip olduğunu ortaya koymuştur. Ayrıca hesaplanan idealite faktörleri doğrultusunda diyot yapısının kalitesi analiz edilerek arayüz özellikleri ve taşınım mekanizmaları hakkında ayrıntılı çıkarımlar yapılmıştır. Elde edilen sonuçlar, sol–jel yöntemiyle üretilen Mo ve W katkılı ZnO ince filmlerin şeffaf elektronikler, diyot yapıları ve gelişmiş algılama teknolojileri için güçlü bir aday malzeme olduğunu göstermektedir.

ANAHTAR KELİMELER: İnce Film, Çinko Oksit, Molibden, Tungsten

TABLE OF CONTENTS

Page

ABSTRACT ..... **iv**

ÖZET ..... **v**

TABLE OF CONTENTS ..... **vi**

LIST OF FIGURES ..... **viii**

LIST OF TABLES ..... **x**

LIST OF ABBREVIATIONS AND SYMBOLS ..... **xi**

ACKNOWLEDGEMENT ..... **xii**

1. INTRODUCTION **1**

1.1 Importance of Thin Films in Electronic and Optical Applications 1

1.2 Properties of ZnO and Reasons for Doping 4

1.2.1 Electrical and Optical Properties of ZnO Structure 5

1.2.2 Doping of ZnO and Fundamental Reasons 6

1.3 Effects of Mo and W dopants 7

1.4 Literature Overview 9

1.5 Aim and Scope of the Study 13

2. THEORETICAL FRAMEWORK **14**

2.1 A p-n Junction 14

2.2 A Schottky Diode 17

2.2.1 Schottky Barrier 23

2.3 Ohmic Contact 25

2.3.1 Ohmic Contact in ZnO and Doped ZnO Thin Films 26

2.4 XRD (X-Ray Diffraction) 28

2.5 Fourier Transform Infrared Spectrometry (FTIR) 29

2.6 I-V Characteristics of a Diode 30

2.7 Ideality Factor of a Diode 31

2.8 Structure and Properties of ZnO 32

2.9 Doping Mechanisms in ZnO 35

2.10 Effects of Mo and W Doping on Optical and Electrical Properties 36

2.11 Fundamentals of the Sol–Gel Method and Coating Process 38

3. MATERIALS AND METHODS **42**

3.1 Preparation of Solution 42

3.2 Preparation of Heterojunctions 47

4. RESULTS **49**

4.1 XRD Results of Doped ZnO Films 49

4.2 I-V Characteristics of ZnO Thin Films 53

4.3 Ideality Factor 54
4.4 Fourier Transform Infrared Spectroscopy (FTIR) Results 55
5. DISCUSSION 58
5.1 XRD Analysis 58
5.2 Electrical Properties 59
5.3 Optical Properties 61
6. CONCLUSION 63
7. REFERENCES 65

LIST OF FIGURES

Page

Figure 1.1. Wurtzite hexagonal structure of ZnO. 5

Figure 2.1. A diode representation including PN junction and diode symbol Image taken from Colinge and Colinge (2002).....15
Figure 2.2. PN junction's current-voltage characteristics. Image taken from Colinge and Colinge (2002). 15
Figure 2.3. N-type and P-type regions' individual energy band diagrams Image taken from Colinge and Colinge (2002).....16
Figure 2.4. PN junction and related energy band diagram Image taken from Colinge and Colinge (2002).....17
Figure 2.5. The one-dimensional representation of the metal–semiconductor contact structure. Image adopted from Sze (1985). 18
Figure 2.6. Energy band diagram of an isolated metal placed next to an isolated n-type semiconductor under non-equilibrium thermal conditions (a). Energy band diagram of a metal–semiconductor contact when the system is in thermal equilibrium (b). 19
Figure 2.7. This graph shows the measured the barrier height for connections between metal and silicon and metal and gallium arsenide Image taken from Image adopted from Sze (1985). 20
Figure 2.8. Energy band diagrams for metal contacts on n-type and p-type semiconductors under various biasing conditions: (a) thermal equilibrium, (b) forward bias, and (c) reverse bias Image taken from Sze (1985). 22
Figure 2.9. Current transport through the thermionic emission process under: (a) thermal equilibrium, (b) forward bias, and (c) reverse bias conditions Image taken from Sze (1985).....24
Figure 2.10. Ohmic contact energy band diagram and Schottky contact energy band diagram.....27
Figure 2.11. Illustration of an X-Ray tube (Öztel, 2019).....28
Figure 2.12. Schematic of X-Ray spectrometer (Öztel et al., 2024).....29
Figure 2.13. A Michelson-Morley interferometer (Öztel et al., 2024). 30
Figure 2.14. Illustration of the band gap of ZnO. 33
Figure 3.1. Before and after photos after catalyst was used.....44
Figure 3.2. Schematic diagram of the production process of Sol-Gel. This sketch was adopted from Oztel (2024).....45

Figure 4.1. Rigaku Multiflex XRD Diffractometer in BAIBU, Bolu, Turkey.....50
Figure 4.2. XRD spectra of 2% Mo doped ZnO thin film. 51
Figure 4.3. XRD spectra of 4% Mo doped ZnO thin film. 51
Figure 4.4. XRD spectra of 1% W doped ZnO thin film. 52
Figure 4.5. 2% Mo doped ZnO/p-Si films I-V measurement results at room temperature.....53
Figure 4.6. 4% Mo doped ZnO/p-Si films I-V measurement results at room temperature.....54
Figure 4.7. 1% W doped ZnO/p-Si films I-V measurement results at room temperature.....54
Figure 4.8. The FTIR analysis of 2% Mo-doped ZnO thin film 55
Figure 4.9. The FTIR analysis of 4% Mo-doped ZnO thin film 56
Figure 4.10. The FTIR analysis of 1% W-doped ZnO thin film.....56

LIST OF TABLES

Page

Table 4.1. Grain size of each films.....52
Table 4.2. Serial resistance and ideality values for each films.....55

LIST OF ABBREVIATIONS AND SYMBOLS

BAIBU : Bolu Abant İzzet Baysal University

EDS : Energy Dispersive Spectroscopy

FTIR : Fourier Transform Infrared Spectroscopy

FWHM : Full width at Half Maximum

IU : Istanbul University

I-V : Current-Voltage

ICDD : International Center for Diffraction Data

LASER : Light Amplification by Stimulated Emission of Radiation

LED : Light Emitting Diode

Pa : Pascal

ppm : Parts per Million

PVD : Physical Vapor Deposition

RCA : Radio Corporation America

SEM : Scanning Electron Microscopy

TCO : Transparent Conductive Oxide

UV : Ultraviolet

XRD : X-Ray Diffraction

ZnO : Zinc-Oxide

ACKNOWLEDGEMENT

I would like to express my deepest gratitude to my advisor, Prof. Dr. Aliekber Aktağ, for his invaluable guidance, insightful comments, and continuous support throughout the development of this dissertation. His expertise and encouragement have been fundamental to the completion of this work.

I would like to extend my sincere appreciation to Assoc. Prof. Dr. Erhan Budak for his valuable assistance and for generously sharing his knowledge with me during the course of this study. His contributions have greatly enhanced the quality and depth of this work.

I am also sincerely thankful to the esteemed members of my dissertation committee; Prof. Dr. Ercan Yılmaz, Prof. Dr. Haydar Arslan and Prof. Dr. Kadir Gökşen for their constructive feedback, valuable suggestions, and the time they devoted to evaluating my research.

I would like to extend my appreciation to Dr. Halim Onur Öztel and Assoc. Prof. Dr. Namık Akçay for their assistance during the experimental phase of this study. Their technical support and contributions significantly enriched the quality of the research.

My heartfelt thanks also go to my friends Dr. Umut Keskin, Dr. Kaan Yüksel Oyulmaz, Özgün Karadeniz, and Dr. Doğan Avcı for their constant encouragement, understanding, and companionship during this challenging process. Their presence has been a great source of motivation.

My sincere thanks go to the Council of Higher Education for their funding and support via the 100/2000 Doctoral Scholarship Program.

To my dear late father…

1. INTRODUCTION

This study aims to synthesize molybdenum 2% and 4% and tungsten 1% and 4% doped zinc oxide (ZnO) thin films using a sol–gel method and to investigate their structural, optical, and electrical properties in detail. The produced films were analyzed via XRD, FTIR, and I–V characterization techniques to evaluate the effects of the doping elements on the band structure, conduction mechanisms, and carrier density. The results demonstrate that Mo and W doping have the potential to enhance performance for ZnO-based opto-electronic applications.

1.1 Importance of Thin Films in Electronic and Optical Applications.

Thin film optical coatings are developed to controllably alter the properties of a surface when applied. The starting point of this process is surface preparation, which significantly affects the coating's effectiveness. Coating can provide thermal, chemical, or environmental benefits, but they are most often used to produce specific optical effects that alter the quality of light without changing its direction. For such coatings to function properly, the substrate surface must be optically smooth, meaning it must be free of any irregularities are smaller than the wavelength of visible light.

Surface cleanliness is even more important than smoothness because the atomic forces holding the thin film together are short-range and can be easily disrupted by a single layer of molecular contamination. Thin film coatings typically consist of one or more very thin layers of selected materials. The combined interference and natural optical properties of these materials provide the desired reflection or transmission characteristics. In some cases, the microstructure of these materials can be modified to enhance their performance and stability.

Optical coatings have been around since antiquity. Melted lead was poured upon glass to increase reflectivity in the earliest mirrors created in the late Roman Empire, but this method fractured the glass and produced tiny, uneven mirrors. Mirrors of almost current quality could be produced by the fifteenth century thanks to the development of flat glass manufacture and the application of tin amalgam coatings. Later in the nineteenth century, chemical silvering became popular, and it

remained so until the 1930s. Anti-reflective glass surfaces and interference-based photographic films were developed at this time thanks to optical experiments.

The modern age of optical coating started in the early 20th century to enhance the functionality of increasingly sophisticated optical instruments. Coating technology was transformed with the introduction of the vacuum deposition technique, which allowed for more accurate control over thin film layers. Due to major developments in the field, optical coatings had quickly expanded by the middle of the 20th century. This was especially true following the development of the laser, which required highly specialized coatings. Although vacuum deposition methods are still frequently employed today, new physical and chemical vapor processes are constantly developing and helping to progress optical technology in the 20th century (Piegari & Flory, 2018).

There are several types of coating materials on any surface such as sputtering and sol-gel method.

Sputtering is the most widely used physical vapor deposition (PVD) techniques for thin film coatings. This method knocks atoms off the surface of the target material by hitting them with high-energy particles (often argon ions) in a vacuum. These displaced atoms gather on the substrate surface to form a homogeneous thin film layer (Mattox, 2010). Sputtering is a common method in optical, electrical, and protective coating applications because it can precisely control coating thickness, deposit a variety of materials together, and produce good adhesive properties (Smith & Hoffman, 1996). Additionally, due to current techniques like magnetron sputtering, high-quality films may be fabricated at lower temperatures and high deposition rates (Wasa & Hayakawa, 1992).

Beginning with metal alkoxides or metal salts, the sol-gel method is a chemical process that quickly changes into a three-dimensional structure and moves into the gel phase after producing colloidal particles known as "sol" in solution (Brinker & Scherer, 1990). This process starts hydrolysis and condensation processes when alkoxides react with water and a solvent. According to Danks et al. (2016), these reactions result in the densification of the network structure and the creation of metal-oxide linkages. Compared to conventional high-temperature ceramic production methods, the sol-gel approach has many advantages. It is possible to make the material uniformly and at low temperatures. Fine-grained,

uniformly distributed structures can be created with this technique, especially when producing oxides like silica, titania, alumina, and zirconia (Merghes et al., 2024).

The three primary steps of this procedure are usually clarity, drying/pyrolysis, and solution preparation. The right catalyst and solvent enable the precursors to be combined during the solution preparation phase. At this stage, the pH, temperature, and molar ratios of the solution directly impact the microstructure of the finished product (Brinker & Scherer, 1990). For instance, although high pH levels speed up condensation and produce a denser structure, low pH levels can speed up hydrolysis while slowing down structure formation. A three-dimensional structure is formed, and the substance becomes viscous during the gelation stage. The structure's homogeneity and porosity are impacted by the gel formation time. Solvents and volatile ingredients are eliminated from the gel during the drying and pyrolysis processes. If these stages are not carefully controlled, pores or cracks may form (Danks et al., 2016).

In terms of materials science, the sol-gel method has several advantages. First, the ability to synthesis at low temperatures allows for the packaging of organic materials that are sensitive to heat while also saving energy (Merghes et al., 2024). Second, materials made using the sol-gel method have a large surface area and a broad porous structure; these characteristics are important for adsorbents, sensors, and catalyst carriers. Furthermore, the chemical flexibility of the sol-gel method makes it simple to incorporate various metal ions or dopants to produce the appropriate chemical features (Bokov et al., 2021). This is a crucial benefit of sol-gel method, particularly for fabricating functional materials with attributes like magnetic or photocatalytic capabilities.

The sol-gel technique has a wide range of applications nowadays. The sol-gel process can be used to create thin film coatings, biomedical implants, optical and magnetic materials, sensors, and energy storage systems (Brinker & Scherer, 1990; Merghes et al., 2024). For instance, self-cleaning surfaces and photocatalytic applications employ titanium-based sol-gel coatings. For drug delivery applications or biological carrier systems, silica-based gel structures offer the perfect setting. Additionally, it is well known that the sol-gel process is useful in creating hybrid organic-inorganic materials, which perform better in terms of mechanical strength and functional qualities (Danks et al., 2016).

The sol-gel method is environmentally friendly. It uses less energy and produces less waste than traditional high-temperature methods. Therefore, the properties of materials obtained using the sol-gel method have recently attracted more attention as a method suitable for green chemistry approaches by controlling the synthesis conditions (Merghes et al., 2024). For example, the gel formation time and drying conditions significantly affect the pore size and distribution. Controlled drying can cause cracking while providing a more uniform pore structure. Additionally, the chemical structure of the molecule is directly influenced by the type of solvent, the molar ratio of water or alkoxide, and the crystal density and mechanical strength of the final material (Bokov et al., 2021).

Therefore, optimizing each parameter in sol-gel synthesis is crucial to obtain materials with properties suitable for the target application.

To sum up, the sol-gel method is an adaptable, low-temperature, and eco-friendly production technique that may be used for materials science research as well as industrial applications. Microstructure control, composition flexibility, coatings, ceramics, biomedical, and energy materials are all excellent uses for this technique(Bokov et al., 2021; Brinker & Scherer, 1990; Danks et al., 2016; Merghes et al., 2024). In this regard, the sol-gel method is particularly noteworthy as a potent technique for generating high-performance materials in real-world applications and new functional materials in basic research.

1.2 Properties of ZnO and Reasons for Doping.

Zinc oxide (ZnO) is a material belonging to the class of II–VI compound semiconductors, characterized by a wide bandgap and a direct bandgap. At room temperature, the band gap is reported to be in the range of approximately 3.2–3.37 eV, and the fact that it has a high exciton binding energy of ~60 meV is noteworthy, as it allows for effective exciton transitions even at room temperature (Özgür et al., 2005; Sood et al., 2025). These fundamental properties of ZnO make it a candidate material for a wide range of applications, including optoelectronics, photonics, sensor technologies, and transparent electronics (Özgür et al., 2005).
In its thermodynamically stable phase, ZnO has a hexagonal wurtzite crystal structure which is shown in Figure 1.1. This structure is closely linked to the material's piezoelectric and pyroelectric properties and has a spatial asymmetry due to the tetrahedral coordination of Zn and O atoms (Özgür et al., 2005). Additionally,

because of its strong chemical and thermal durability, comparatively low cost, and environmentally friendly (non-toxic) structure, ZnO is favored in industrial applications (Xiu et al., 2016). Because of its high melting point and mechanical hardness, ZnO is also a good choice for coatings that need to be resistant to wear. In terms of electrical activity, ZnO primarily displays intrinsic n-type behavior, which is linked to natural flaws like oxygen vacancies and zinc interstitials (Özgür et al., 2005).

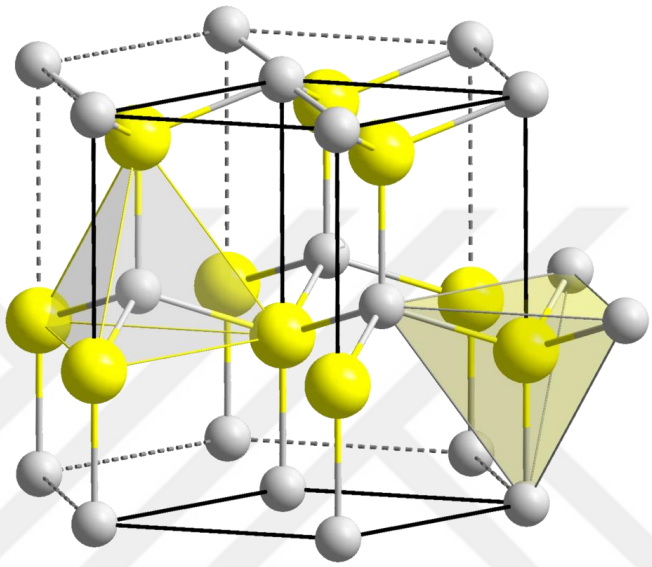

Figure 1.1. Wurtzite hexagonal structure of ZnO.

1.2.1 Electrtical and Optical Proporties of ZnO Structure

ZnO thin films have strong absorption and/or emission capabilities in the ultraviolet (UV) region and good optical transparency (>80–90%) throughout the visible spectrum (Jiamprasertboon et al., 2019; Koç, 2021). ZnO is therefore extensively researched in optoelectronic devices, such as solar cells, LEDs, laser diodes, UV photodetectors, and transparent conductive oxide (TCO) electrodes (Özgür et al., 2005).

ZnO may be generated electrically over a broad resistivity range (about 10^{-3}–10^{1} Ω·cm). This broad range is dependent on doping conditions, oxygen partial pressure, and production method (Özgür et al., 2005). Low resistivity and high optical transparency are desired in transparent conductive oxide applications; doping tactics are strongly related to this need (Liu et al., 2013).

1.2.2 Doping of ZnO and Fundamental Reasons

For ZnO to reach the required performance level in many applications, controlled doping is essential. The following succinctly describes the primary advantages of doping:

Enhanced Electrical Conductivity

ZnO is required to have high carrier concentration and mobility for thin-film devices and TCO applications. By raising the free electron density, doping ZnO with group III elements (Al, Ga, In, B, etc.) often increases conductivity (Alsaad et al., 2020; Zhai et al., 2016).

For instance, it has been noted that when the Al doping ratio rises in ZnO:Al films, the optical bandgap and carrier density both rise while the visible area transmittance remains over 85% (Zhai et al., 2016).

Bandgap Engineering

Another key reason to modify ZnO's bandgap for certain uses is bandgap tuning. According to Alsaad et al. (2020) and Sygletou et al. (2022) doping can either narrow or widen the bandgap through changes in lattice characteristics or cause a widening of the bandgap due to the Burstein–Moss effect (filling of the conduction band due to high electron density). For instance, it has been shown that increasing Al doping raises the effective bandgap and causes the absorption edge of ZnO thin films to shift to shorter wavelengths (blue shift) (Zhai et al., 2016). On the other hand, some metal additives can cause a slight narrowing of the band gap and a red shift in the optical absorption edge.

Control of Carrier Type and Concentration

Doping experiments (with acceptor dopants like N, P, and As) targeted at generating p-type ZnO are being thoroughly investigated, despite the fact that ZnO normally displays n-type behavior because to inherent defects (Özgür et al., 2005). However, the presence of self-compensating defects, deep acceptor levels, and problems with thermodynamic stability make creating p-type ZnO challenging. On the other hand, n-type doping (Al, Ga, In, F, H, etc.) is widely employed and comparatively more successful, especially for diode/Schottky contact engineering and transparent conductive (Alsaad et al., 2020).

Improvement of Structural and Morphological Properties

Doping influences microstructural parameters such grain size, degree of crystallization, surface roughness, and film density in addition to electrical and optical properties. While some dopants can increase defect density and scattering centers, others can improve preferred orientations and crystal quality (Huber et al., 2019; Mary & Arumugam, 2017). Grain size and surface roughness of ZnO thin films have been found to vary significantly depending on the molarity or additive concentration (Koç, 2021; Mary & Arumugam, 2017).

In conclusion, because of its wide bandgap, high exciton binding energy, high visible region transmittance, chemical/thermal stability, and environmental friendliness, ZnO is a semiconductor material that stands out in new-generation optoelectronic and transparent electronic applications (Özgür et al., 2005). However, controlling ZnO's electrical, optical, and structural characteristics is crucial to achieving the required performance level in various applications; hence, suitable doping techniques must be developed. The efficiency and stability of ZnO-based devices are directly determined by doping, which enables the engineering of the carrier density, bandgap, transparency-conductivity balance, and film microstructure in the desired direction (Ahmad et al., 2025).

1.3 Effects of Mo and W dopants.

In studies on zinc-oxide (ZnO) used as a semiconductor, it is crucial to enhance the electrical, optical, and structural properties of the materials through doping. The effect of transition metal dopants such as molybdenum (Mo) and tungsten (W) in ZnO thin film systems is important both in terms of fundamental material physics and application. The structural, optical, and electrical effects of Mo and W dopants on ZnO will be discussed in this part (Ganesh et al., 2022; Jalal et al., 2024).Research on Mo-doped ZnO systems using X-ray diffraction (XRD) has shown that crystallite diameters decrease as dopant concentration increases. For example, ZnO's crystallite size decreased as the Mo content increased, leading to a bigger surface area and higher grain boundary effects (Ganesh et al., 2022). Additionally, a number of investigations have shown that Mo is integrated into the ZnO lattice and that Mo input generates new energy levels instead of Zn.

Mo doping affects the light absorption edge and bandgap of ZnO. In the study by Ganesh et al. (2022), it was reported that the bandgap narrowed in Mo-

doped ZnO nanoparticles depending on the doping amount. Such bandgap narrowing is interpreted as the opposite of the Burstein–Moss effect or as the effect of the intermediate bands formed by doping. Furthermore, transmittance measurements showed that high optical transmittance is maintained in Mo-doped films.

Mo doping has the potential to improve conductivity by increasing the free carrier concentration. For example, in a study, the average visible region transmittance of a ZnO film doped by 1 at.% Mo was measured to be ~87%, and it was suggested that these systems are suitable for transparent conductive oxide (TCO) applications. However, at high Mo doping levels, adverse effects such as structural distortion, grain boundary increase, or second phase formation may be observed, which can reduce carrier mobility (Bancheva-Koleva et al., 2024).

Because of their high transmittance and low resistance, Mo-doped ZnO thin films are particularly attractive options for solar cells, transparent electrodes, and photocatalytic systems. Mo-doped ZnO nanoparticles shown great efficiency in the electrocatalytic degradation of Rhodamine B solution, according to Ganesh et al. (2022)

Structural strain and crystal distortion are important parameters in W-doped ZnO films. In a study Zhang et al. (2013) it was reported that as the W doping increased, the strain in the ZnO film decreased, oxygen vacancies increased, and the carrier density rise. Furthermore, Vines et al. (2018) suggested that 1-2 at.% W doping could lead to changes in the magnetic and electrical behavior of the ZnO lattice.

In particular, optical transmittance and electrical conductivity are balanced in W-doped ZnO systems. ZnO/Si heterojunction photodetectors doped with 2% W are shown to exhibit an average visible transmittance of 83.6% and a high sensitivity of 3.84 A/W. This result suggests that W doping improves carrier separation and reduces recombination rates (Jalal et al., 2024)

The W content must be optimized for ideal performance. In particular, a high content ratio can reduce film quality. Therefore, the production method, annealing temperature, and content ratio must be evaluated together (Sales Amalraj et al., 2022). W-doped ZnO films are particularly suitable for UV photodetectors, transparent electronics, and high-speed optoelectronic devices. Jalal et al. (2024)

provided concrete data on the high performance of such a W-ZnO/Si device in their study.

Both Mo and W dopants have positive effects on carrier concentration and optical/electrical performance in ZnO systems; however, which dopant is more suitable in which context depends on the operating conditions. For example:

Mo doping is particularly strong in terms of electrical conductivity and use as a transparent conductive oxide, but crystal quality may decrease as the doping concentration increases.

W doping appears to be effective in improving carrier separation and device performance; however, synthesis parameters and doping concentration must be carefully selected.

Both dopants have the potential to further improve the original n-type nature of ZnO in terms of carrier concentration. This is critical for thin-film device applications.

ZnO systems doped with Mo and W show potential for high-performance optoelectronic devices in thin-film technology. The crystal structure, carrier density, optical transmittance, and device characteristics can all be drastically changed by doping. The compatibility of factors including doping ratio, film production technique, and annealing conditions, however, is crucial for success. As a result, it is crucial to discuss how these two dopants affect ZnO in your thesis, taking into account both the literature and your own experimental setup.

1.4 Literature Overview

In recent years, research on oxide semiconductors has focused on improving the electrical, structural, and optical properties of thin films based on ZnO (zinc oxide). ZnO has a band gap ≈3.37 eV, that is means high exciton binding energy, chemical stability, and low temperature fabricability, ZnO has a several applications, from photodetectors and transparent conductive oxides to gas sensors and heterojunction diodes. However, it is known that the carrier density, electrical conductivity, and crystallinity of pure ZnO thin films do not fully meet the application requirements (Liu et al., 2013). Therefore, many studies have investigated the modification of ZnO with different metal dopants to improve its performance at room temperature and above. While Group III elements such as Al, Ga, and In have been frequently preferred for doping for many years, there is

considerable debate regarding the lattice deformations and crystal defects that arise from differences in the ionic radius of these dopants. In this context, how high-valent metal dopants such as transition metals molybdenum (Mo) and tungsten (W) affect the electronic band structure of ZnO has become an important research area.

Although doping with Group III elements such as Al, Ga, and In has been preferred for many years, there are also findings that these dopants increase the deformation effects and crystal defects on the ZnO lattice (Singh et al., 2019). Therefore, dopants such as molybdenum (Mo) and tungsten (W), which are higher-valent transition metals, have attracted attention in recent years. In particular, the substitution of Mo^{6+} and W^{6+} ions in the lattice instead of Zn^{2+} ions contribute to a significant improvement in n-type conductivity by providing higher free electron density (Chen et al., 2024). The improvements in structural and electrical properties provided by such dopants depend on the doping ratio, the production method, and the thin film morphology. In this context, the 2% and 4% Mo doping and 1% W doping preferred in this study offer a meaningful investigation range in the literature from both experimental and theoretical perspectives.

It has been reported that Mo-doped ZnO thin films exhibit high crystalline integrity, especially at low doping concentrations, while a slight broadening occurs in the optical bandgap (Xu et al., 2011).The fundamental reason for this is that Mo^{6+} ions provide a higher valence structure in the ZnO lattice, thereby increasing the carrier density. The literature shows that the Mo doping concentration has mostly been investigated in the range of 0.5–3 at.% (Mekki & Tabet, 2014). Therefore, a 4% Mo doping level is a relatively understudied doping level in the literature, making it a unique value for you to thoroughly evaluate the effects of doping on crystal structure, defect mechanisms, and electrical carrier behavior. At the same time, the 2% Mo ratio is compatible with the optimal high-valency doping ranges and allows for comparison with reference points in the literature. Thus, your thesis evaluates both well-known and less researched doping levels under the same umbrella regarding how Mo doping ratios alter the physical properties of ZnO, thereby contributing to the literature in this regard.

Studies on W-doped ZnO thin films are more limited compared to Mo doping and have mostly been conducted at low concentrations of 1–2% (Qiu, 2025).It has been reported that W doping increases the electrical conductivity of ZnO, causes a slight broadening of the optical band structure, and improves

performance, particularly in UV photodetector applications. However, it has been stated that high concentrations of W doping can increase crystal structure defects. Therefore, 1% W doping is scientifically significant both in terms of providing an optimal doping level and enabling comparative analysis with Mo doping. Studies in literature that systematically compare Mo and W doping within the same thesis are quite rare. This makes this research original and contributes to a holistic understanding of the reactions of ZnO to high-valent metal doping.

When the crystal structure of ZnO is examined, it has been confirmed in many studies that the wurtzite hexagonal phase is preserved even after Mo and W doping (Amakali et al., 2020). However, with increasing doping ratio, shifts in XRD peaks are observed, slight changes in lattice constants occur, and the strain state of the thin film may change accordingly. Literature indicates that Mo and W dopants cause less deformation compared to dopants such as Al and Ga due to their values close to the Zn^{2+} ionic radius (Mekki & Tabet, 2014). This allows for higher crystalline quality in thin films. However, it has also been shown that high-valent dopants can cause an increase in defect types such as oxygen vacancies (V_O) and zinc interstitials (Zn_i) (Chen & Jian, 2016). In this context, the optical and electrical data and XRD results that you will analyze in your study will provide an important finding in determining the relationship between the doping ratios, defect formation and crystal structure.

In terms of electrical properties, Mo and W doping increases the free carrier density of ZnO and, consequently, improves its electrical conductivity. However, this improvement is dependent on the doping rate; it has been reported that carrier scattering increases and mobility can decrease at higher doping (Shaw et al., 2015). The increase in carrier density achieved with Mo and W doping causes the Burstein–Moss effect, which leads to a widening of the optical band gap depending on the doping rate (Qiu, 2025). It has been reported in the literature that this effect is particularly evident with high-valent dopants such as Mo and W. Therefore, the band gap changes expected in your thesis will not only confirm the doping mechanism but also scientifically demonstrate the relationship between the increase in carrier concentration of ZnO and its optical behavior.

It has been reported that Mo-doped ZnO thin films exhibit high crystalline integrity, especially at low doping concentrations, while a slight broadening occurs in the optical bandgap (Mekki & Tabet, 2014). The fundamental reason for this is

that Mo^{6+} ions provide a higher valence structure in the ZnO lattice, thereby increasing the carrier density. The literature shows that the Mo doping concentration has mostly been investigated in the range of 0.5–3 at % (Mekki & Tabet, 2014). Therefore, a 4% Mo doping level is a relatively understudied doping level in literature, making it unique value for you to thoroughly evaluate the effects of doping on crystal structure, defect mechanisms, and electrical carrier behavior. At the same time, the 2% Mo ratio is compatible with the optimal high-valency doping ranges and allows for comparison with reference points in the literature. Thus, your thesis evaluates both well-known and less researched doping levels under the same umbrella regarding how Mo doping ratios alter the physical properties of ZnO, thereby contributing to the literature in this regard.

Another important element that enhances the originality of this thesis is the systematic investigation of two different Mo doping ratios (2% and 4%) and the comparison of the results with W doping (1%). While studies in the literature mostly focus on a single doping element, this study fills a significant gap in literature by evaluating the effects of both elements on ZnO thin films within a single framework. Furthermore, fabricating diodes from the resulting thin films provides depth not only in terms of material characterization but also in terms of application. Diode structures based on ZnO doped with Mo or W have been studied in the literature only a limited number of times, and the effects of doping ratios on diode parameters, in particular, remain a topic that needs to be investigated (Khan et al., 2020). Therefore, the parameters such as rectification ratio, barrier height, and series resistance obtained in this study are both original and contribute to literature.

In conclusion, although various studies on the structural, electrical, and optical properties of Mo- and W-doped ZnO thin films exist in the literature, these studies have mostly focused on limited doping ranges. The systematic evaluation of 2% and 4% Mo doping, comparison with 1% W doping, and application of the resulting films in diode structures in this thesis fills the gaps in the literature and contributes to a comprehensive understanding of the effects of high-valent transition metal doping on ZnO. In this respect, the study is highly original from both scientific and practical perspectives and adds value to the development of ZnO-based electronic devices.

1.5 Aim and Scope of the Study

The aim of this study is to comparatively investigate the structural, electrical, and optical properties of ZnO thin films doped with 2% and 4% molybdenum (Mo) and 1% tungsten (W) and to comprehensively demonstrate the effects of these doping agents on the semiconductor characteristics of ZnO. The crystallinity, band gap modification, carrier density, diode behavior, and interface properties of the produced thin films are analyzed in detail, thus providing a scientific basis for the integration of high-valent transition metals into ZnO-based electronic devices. The findings obtained in this context are intended to complement the limited Mo–W-doped ZnO studies in the literature and to contribute to the development of ZnO-based diode technologies.

2. THEORETICAL FRAMEWORK

2.1 A p-n Junction

One of the basic components of basic semiconductor structures, the p-n junction (P-type/N-type semiconductor junction), will be covered first in this section. Next, the metal–semiconductor junction known as the Schottky diode will be discussed. Both the physical structure and the features of the device depend on this differentiation. Gaining an understanding of these subjects is very helpful for comprehending the working principles and potential applications of gadgets in a project at any academic study (Colinge & Colinge, 2002).

A PN junction is created when a P-type semiconductor meets an n-type semiconductor. This junction is referred to as a homojunction if the n-type and p-type areas are composed of the same semiconductor material (for example, n-type silicon and p-type silicon). This junction is referred to as a heterojunction if the semiconductor materials are different for example, p-type silicon and p-type germanium (Colinge & Colinge, 2002).

A single PN junction makes up a diode, a semiconductor device (Figure below). It is usually employed as a rectifying element and has a very nonlinear current-voltage profile in contrast to a resistor. Light-emitting diodes (LEDs) and laser diodes are two types of diodes that may emit light and laser light, respectively. A bipolar transistor is a device that may enhance electrical signals when two PN junctions are properly combined. One of the characteristics of a PN junction is that current can flow in one direction but not the other side. It functions as a rectifier as a result. The Figure 2.1 displays the sign (direction) used in this section (Colinge & Colinge, 2002).

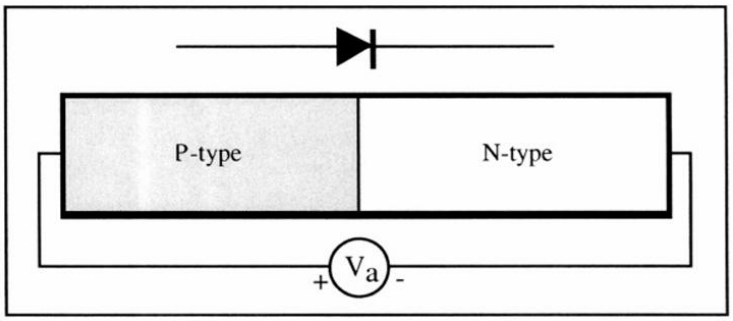

Figure 2.1. A diode representation including PN junction and diode symbol Image taken from Colinge and Colinge (2002).

It is regarded as positive if the applied voltage is greater on the P side than the N side. As seen in Figure 2.2, current passes through the diode when the voltage is positive but not when it is negative.

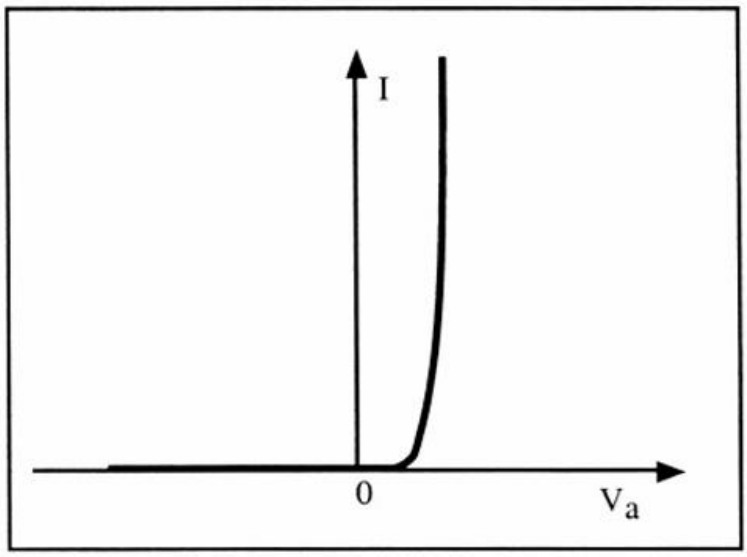

Figure 2.2. PN junction's current-voltage characteristics. Image taken from Colinge and Colinge (2002).

By applying positive voltage, that means the diode is forward biased. For negative voltage that means the diode is reverse biased. The current of a diode can be expressed by the following equation,

$$I = I_s \left(exp \left[\frac{qv_a}{kT} \right] - 1 \right) \tag{2.1}$$

where, I_s is a constant and V_a is the applied voltage.

An analog of a diode is a valve that regulates liquid flow. The valve opens to let the liquid flow when a pressure differential is supplied in the forward direction. However, if the pressure difference is applied in the opposite direction, the valve closes and there is no liquid flow; if the valve is flawed or has a slightly "leaky" structure, only a few drops may pass (Colinge & Colinge, 2002).

$$E_{FN} - E_i = kT \ln\left(\frac{N_d}{n_i}\right) \qquad \text{For N-Region} \qquad (2.2)$$

$$E_i - E_{FP} = kT \ln\left(\frac{N_a}{n_i}\right) \qquad \text{For P-Region} \qquad (2.3)$$

Now, let us consider a PN junction in thermodynamic equilibrium, that is, with no external bias applied. First, we will examine the p-type and n-type regions separately, as if they were two independent pieces of semiconductor material. For simplicity, we assume that the doping concentrations in both regions are constant N_D in the n-type region and N_A in the p-type region. The energy band diagram of these two semiconductor pieces is shown in the Figure 2.3 below (Colinge & Colinge, 2002).

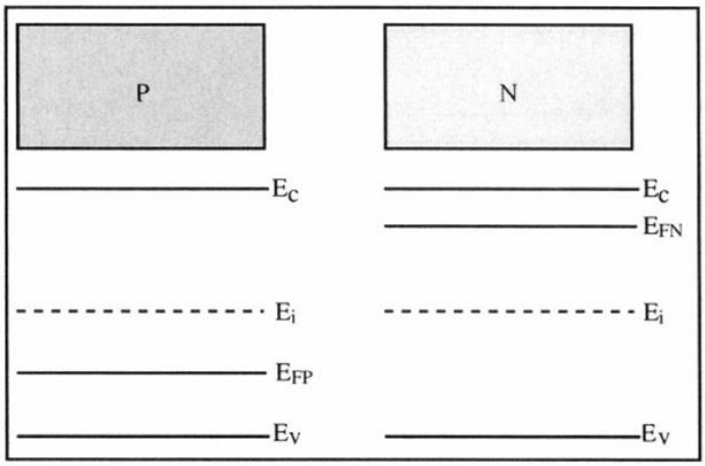

Figure 2.3. N-type and P-type regions' individual energy band diagrams Image taken from Colinge and Colinge (2002).

Let's now combine the p-type and n-type regions to form a PN junction. "Metallurgical junction" refers to the surface where the contact takes place. Step junctions are those when the doping concentration suddenly shifts from p-type to n-type.

The Fermi level of a structure at equilibrium is distinct and constant. As a result, electrons quickly moved from the electron-rich n-type region to the electron-poor p-type region; holes in the p-type material also moved in the direction of the n-type region (Colinge & Colinge, 2002).

An internal potential difference known as the "junction potential" is created in the junction region because of this charge transfer. This situation is illustrated in Figure 2.4 below.

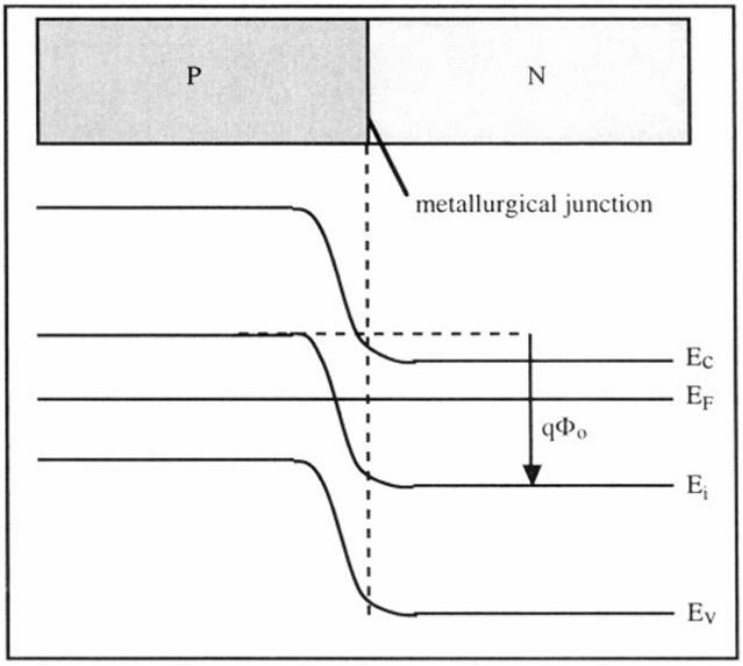

Figure 2.4. PN junction and related energy band diagram Image taken from Colinge and Colinge (2002).

The junction potential, when scaled by the elementary charge $-q$, quantitatively represents the curvature of the semiconductor energy bands. Φ is junction potential can be calculated by the following equation;

$$E_{FN} - E_{FP} = q\Phi_0 = kT\ \ln\left(\frac{N_d}{n_i}\right) + kT\ \ln\left(\frac{N_a}{n_i}\right) = \ kT\ \ln\left(\frac{N_a N_d}{n_i^2}\right) \quad (2.4)$$

$$\Phi_0 = \frac{kT}{q}\ \ln\left(\frac{N_a N_d}{n_i^2}\right). \quad (2.5)$$

2.2 A Schottky Diode

The first practical semiconductor device was a point-contact rectifier, which consists of a metal–semiconductor contact; that is, it has a metallic whisker pressed

against a semiconductor surface. Since 1904, this device has been used in many different contexts. The Schottky barrier is a model that was established based on Schottky's 1938 proposal that rectifying behavior could be driven by a potential barrier created by stable space charges within the semiconductor. Not all metal-semiconductor contacts have rectifying characteristics; in certain instances, the contact shows very little resistance regardless of the applied voltage's polarity; these contacts are known as ohmic contacts. Ohmic contacts are necessary for all semiconductor devices and integrated circuits to link to other parts of electronic systems. In this regard, rectifying and ohmic metal-semiconductor contacts' energy band diagrams and current-voltage properties are investigated (Sze, 1985).

Point-contact rectifiers' features cannot be replicated across different devices. Either a straightforward mechanical contact or an electrical discharge procedure that can produce a tiny, alloyed p-n junction can be used to establish contact.

The primary benefit of point-contact rectifiers is their extremely small surface area, which makes it possible to produce extremely low capacitance, a highly sought-after characteristic for microwave applications.

However, factors like whisker pressure, contact area, crystal structure, the pressure exerted by a thin metal wire, and heating or shaping procedures can vary greatly in various kinds of rectifiers. Because of this, metal-semiconductor contact rectifiers made with planar production techniques have essentially taken their place (Sze, 1985).

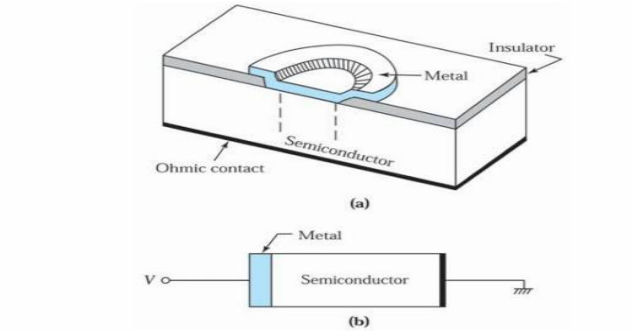

Figure 2.5. The one-dimensional representation of the metal–semiconductor contact structure. Image adopted from Sze (1985).

The schematic shown in Figure 2.5 above displays a schematic diagram of such a device. The gadget is made by first opening a window in an oxide layer and

then depositing a metal layer in a vacuum. Next, a lithography (photolithography) procedure is used to define the metal layer covering the window. The middle area between the dotted lines corresponds to the one-dimensional structure of the metal-semiconductor contact which depicted in Figure 2.6 below.

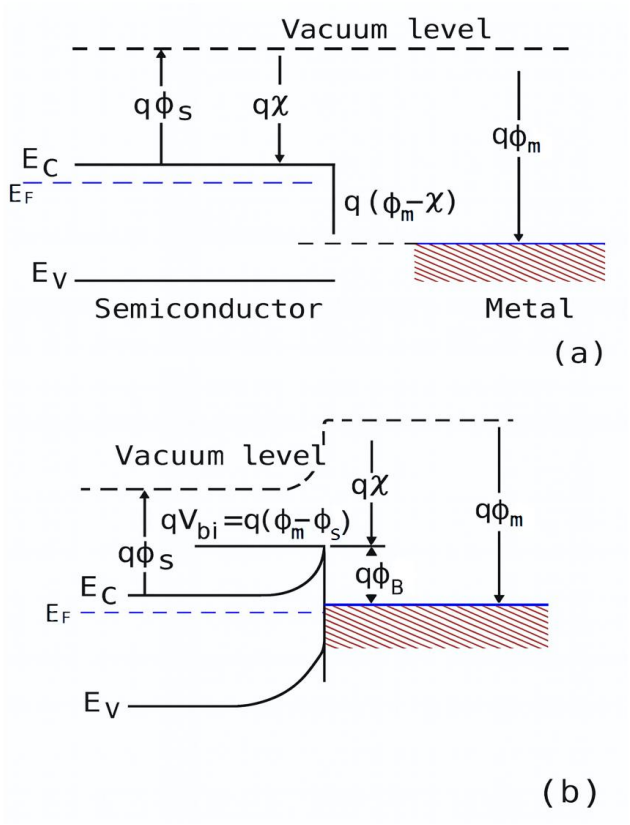

Figure 2.6. Energy band diagram of an isolated metal placed next to an isolated n-type semiconductor under non-equilibrium thermal conditions (a). Energy band diagram of a metal–semiconductor contact when the system is in thermal equilibrium (b).

In this ideal scenario, the barrier height is defined as the difference between the metal's work function and the semiconductor's electron affinity.

$$\Phi_{Bn} = \mathrm{q}\Phi_m - q\chi \tag{2.6}$$

Likewise, for an ideal contact between a metal and a p-type semiconductor, the barrier height can be expressed as follows:

$$\Phi_{Bp} = E_g - (q\phi_m - q\chi) \tag{2.7}$$

where $E_g$is the band gap of the semiconductor. So, barrier heights of the sum of both p and n type semiconductors should be equal to the band gap.

On the semiconductor side of the Figure 2.6, V_{bi} represents the built-in potential experienced by electrons in the conduction band as they attempt to move into the metal.

$$V_{bi} = \phi_{Bn} - V_n \tag{2.8}$$

Those potentials in the order of electron volts except ϕ_{Bn} which is barrier height is in volts. The barrier height and bias effects formed at the metal–semiconductor interface (Schottky diode) can be explained like the following descriptions.

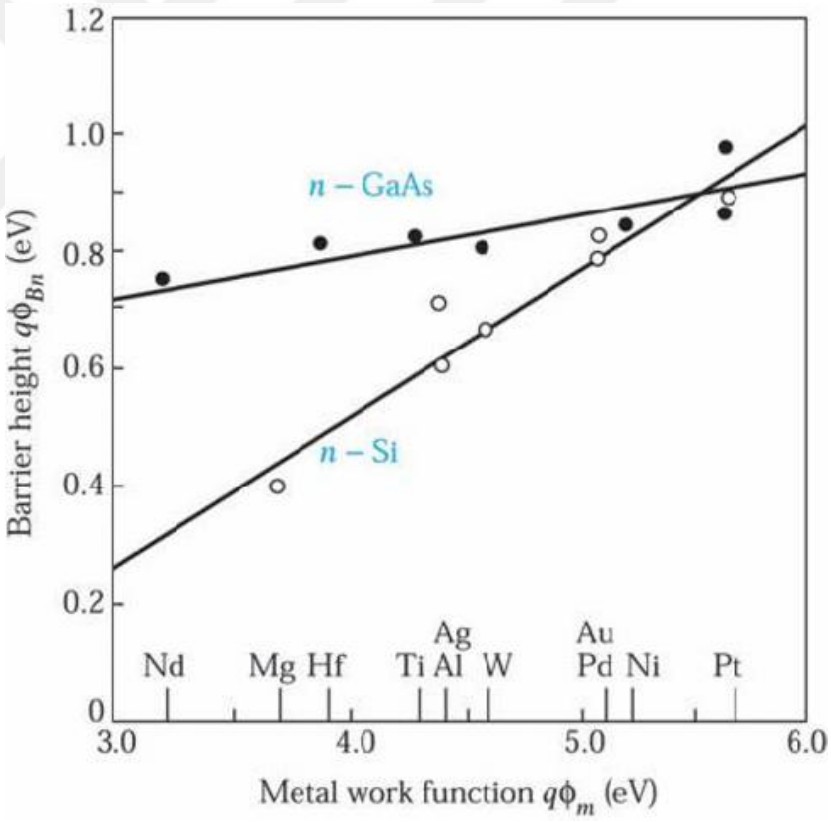

Figure 2.7. This graph shows the measured the barrier height for connections between metal and silicon and metal and gallium arsenide Image taken from Image adopted from Sze (1985).

The observed barrier heights for n-type silicon and n-type gallium arsenide are displayed in Figure 2.7. Because surface energy levels within the forbidden energy band are created by crystal lattice distortions on the semiconductor surface, the observed dependency is not as significant as the equations suggest. The actual barrier height is influenced by these surface states, which function as donors or acceptors. Under zero-bias conditions (thermal equilibrium), the Fermi levels of both materials are aligned. When a forward bias is applied, the barrier height is reduced by this amount, facilitating the transfer of electrons into the metal. When a reverse bias is applied, the barrier height increases by V_r, making electron transport more difficult. The p-type semiconductor has a similar phenomenon, but the polarity is inverted. Figure 2.8 illustrates the charge and electric field distributions in a metal–semiconductor contact.

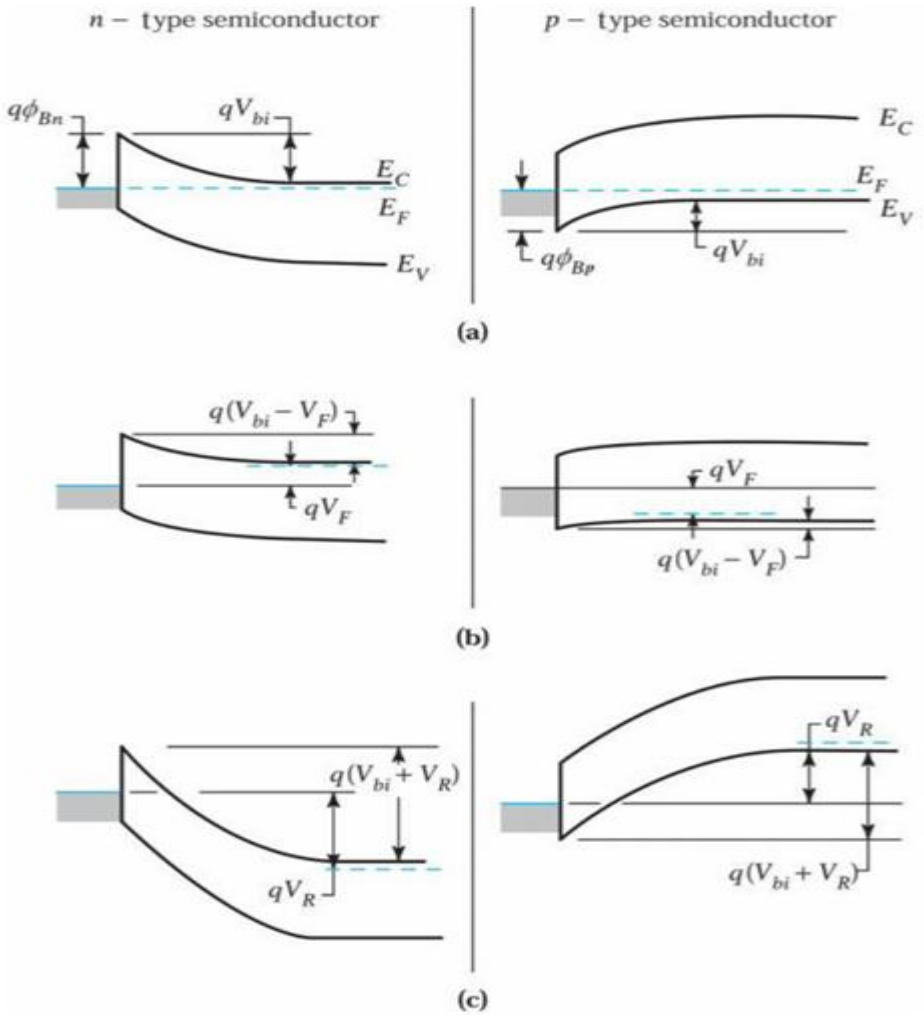

Figure 2.8. Energy band diagrams for metal contacts on n-type and p-type semiconductors under various biasing conditions: (a) thermal equilibrium, (b) forward bias, and (c) reversebias Image taken from Sze (1985).

The metal is assumed to be a perfect conductor, so the transferred charge accumulates within a very narrow region at the metal surface. On the semiconductor side, the space-charge region extends over a width W, and the resulting charge distribution is identical to that of a one-sided abrupt p^+–n junction. The electric field decreases linearly with increasing distance, reaching its maximum value E_m at the interface. Thus, the electric field distribution can be expressed as follows:

$$|\varepsilon(x)| = \frac{qN_D}{\varepsilon_s}(w - x) = \varepsilon_m - \frac{qN_D}{\varepsilon_s}x \tag{2.9}$$

$$\varepsilon_m = \frac{qN_D W}{\varepsilon_s} \tag{2.10}$$

Assume that ε_s is dielectric permittivity of the certain semiconductor. The voltage across the space-charge region—corresponding to the area beneath the electric field curve in Figure 2.8(b) is given by;

$$V_{bi} - V = \frac{\varepsilon_m W}{2} = \frac{qN_D W^2}{2\varepsilon_s} \tag{2.11}$$

$$W = \sqrt{2\varepsilon(V_{bi} - V)/qN_d}\ . \tag{2.12}$$

Where W is the depletion layer can be expressed as the Eqn. 2.12. Then the space-charge density can be given as;

$$Q_{sc} = qN_D W = \sqrt{2q\varepsilon_s N_D (V_{bi} - V)} C/cm^2\ . \tag{2.13}$$

2.2.1 Schottky Barrier

A Schottky barrier denotes a metal–semiconductor interface characterized by a barrier height significantly exceeding kT, along with a doping concentration sufficiently low compared to the density of states in either the conduction or valence band. While minority carriers are mostly responsible for conduction at p–n junctions, majority carriers are mostly responsible for current transfer in a Schottky barrier. Thermionic emission of majority carriers from the semiconductor across the potential barrier into the metal is the predominant transport mechanism in Schottky diodes operating at moderate temperatures (e.g., 300 K).

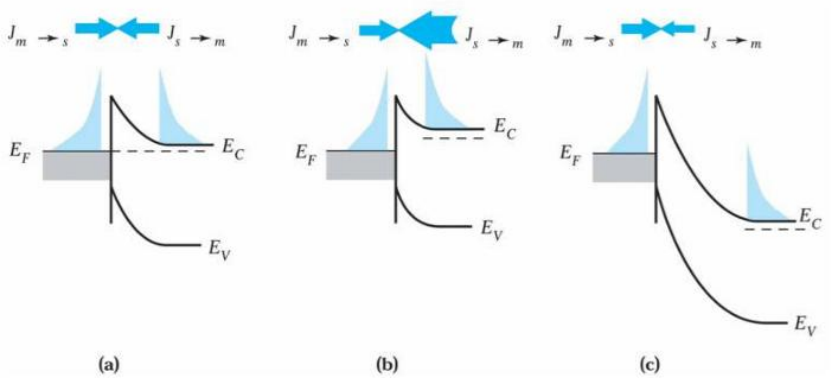

Figure 2.9. Current transport through the thermionic emission process under: (a) thermal equilibrium, (b) forward bias, and (c) reverse bias conditions Image taken from Sze (1985).

The process of thermionic emission is demonstrated. The net current is zero in thermal equilibrium which is shown in Figure 2.9, where the current density is established by balancing two carrier flows that are opposite in direction and of equal size. There is a balanced electron flow from the metal toward the semiconductor in response to the semiconductor's tendency for electrons to flow (or spread) toward the metal. The electron density at the boundary determines the proportion of these current components. Now the work function can be written that way;

$$n_{th} = N_c exp\left(-\frac{q\phi_{Bn}}{kT}\right), \tag{2.14}$$

Where N_c is the density of states for the conduction band, then current between metal and semiconductor becomes,

$$|J_{m\to s}| = |J_{s\to m}| = C_1 N_c exp\left(-\frac{q\phi_{Bn}}{kT}\right), \tag{2.15}$$

where $J_{m\to s}$ represents the current from metal part to the semiconductor, moreover $J_{s\to m}$ means the current from semiconductor side to the metal side. It is clearly seen that the magnitude of the current for each side is equal to themselves. as we look closer into the Figure 2.9(b) the voltage for forward biased diode the static potential between the barriers can be reduced, then the density of the electron at all surface increases according to the Eqn. 2.16 below;

$$n_{th} = N_c exp\left(-\frac{q(\phi_{Bn}-V_F)}{kT}\right). \quad (2.16)$$

Therefore, the current generated between the metal-semiconductor interface by the flow of electrons through the semiconductor is modified by the same factor shown in Figure 2.9(b). In contrast, the electron flow from the metal to the semiconductor remains constant because the potential barrier maintains its equilibrium value.

$$J = J_{s\to m} - J_{m\to s} \quad (2.17)$$

$$= C_1 N_c exp\left(-\frac{q(\phi_{Bn}-V_F)}{kT}\right) - C_1 N_c exp\left(-\frac{q\phi_{Bn}}{kT}\right) \quad (2.18)$$

$$= C_1 N_c e^{-q\phi_{Bn}/kT}\left(e^{qV_F/kT} - 1\right) \quad (2.19)$$

Accordingly, the current–voltage relation of a metal–semiconductor contact under thermionic emission conditions is given by;

$$J = J_s\left(e^{qV_F/kT} - 1\right) \quad (2.20)$$

$$J = A^* T^2\left(e^{-q\phi_{Bn}/kT}\right) \quad (2.21)$$

Assuming, J_s is the saturation current density, then the V is the applied potential for each forward and reverse bias.

2.3 Ohmic Contact

Metal-semiconductor interfaces are one of the most important factors in semiconductor technology that affects an electronic device's performance. These interfaces allow for carrier injections and establish the device's electrical connection to the external circuit. The two main types of metal-semiconductor contacts are (1) Schottky contacts with rectifying characteristics and (2) Ohmic contacts that conduct current linearly in both directions. An electrical interface with low contact resistance that ideally displays symmetric and linear current-voltage (I–V) behavior is known as an Ohmic contact. Ohmic contact happens when the potential barrier on the semiconductor surface offers little resistance to carrier transport, according to (Ng & Sze, 2007).

The energy band alignment between the semiconductor and the metal is the foundation of the ohmic contact theory. The barrier height that could stop electrons from moving from the metal to the semiconductor is at a minimum in n-type semiconductors when the metal's work function is less than the semiconductor's electron affinity. In this instance, carriers can freely flow through the interface even at low voltage since the energy band diagram is nearly flat. On the other hand, carrier transport can only occur through tunneling or thermionic emission if the barrier height is too high. Thermionic emission predominates in low-barrier contacts when studying temperature-dependent carrier transport processes, but the tunneling mechanism emerges at high dopant concentration. Heavy doping of the semiconductor surface causes the depletion zone to narrow, facilitating quantum tunneling and enabling Ohmic activity at the metal-semiconductor interface (Tung, 2014).

Understanding Ohmic and Schottky contacts is easier with energy band diagrams. When metal meets an n-type semiconductor, charge carriers redistribute to align Fermi levels. When the metal has a low work function, downward band bending appears on the semiconductor surface. This facilitates the formation of an Ohmic contact. In contrast, when the metal’s work function exceeds that of the semiconductor, upward band bending is observed, leading to the formation of a Schottky barrier (Pierret, 1996).

2.3.1 Ohmic Contact in ZnO and Doped ZnO Thin Films

Because of its large bandgap and rapid electron mobility, ZnO is widely used in optoelectronic applications. On the other hand, Schottky behavior is usually seen in pure ZnO. In order to achieve ohmic contact, surface modification, metal selection, and doping are necessary. By increasing the free electron density, W or Mo doping enables carriers to tunnel through the barrier. Ti/ZnO contacts provide very low contact resistance values, as shown by (Kim et al., 2005).

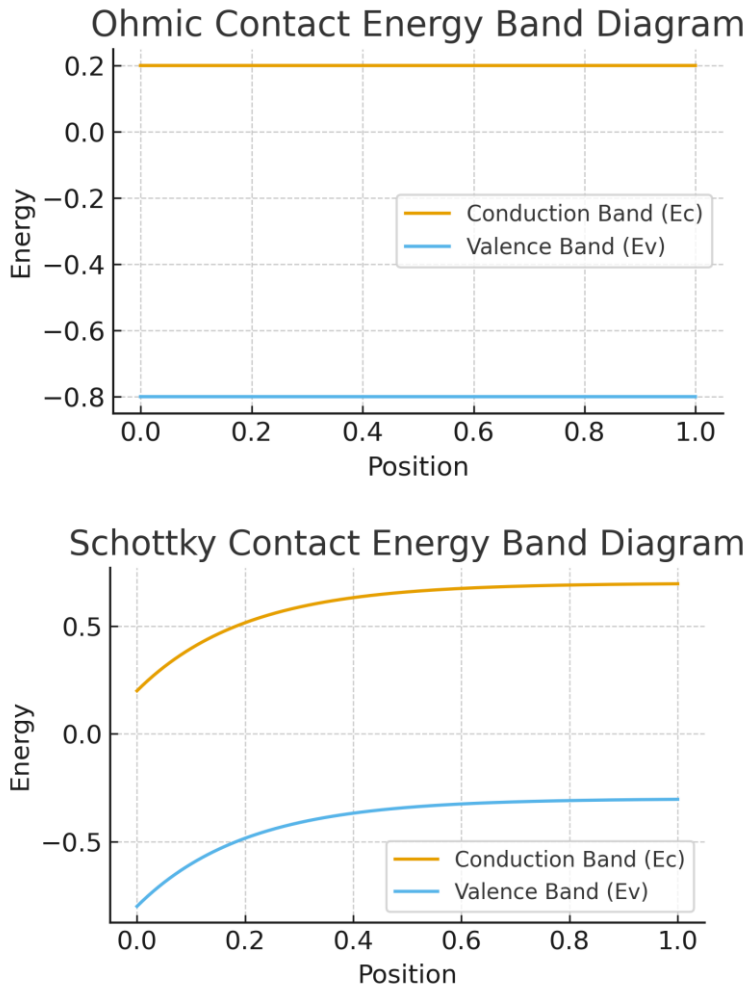

Figure 2.10. Ohmic contact energy band diagram and Schottky contact energy band diagram

In Figure 2.10 shows the energy band diagram of metal semiconductor contacts. Energy band diagrams are essential to comprehending Schottky and Ohmic contacts. Charge carriers are redistributed to change their Fermi levels when a metal meets with an n-type semiconductor. A downward band bending develops on the semiconductor surface if the metal has a low work function. This encourages an Ohmic contact to form (Sze, 1985).

Ohmic contact formation is based on four fundamental physical mechanisms. High doping concentration narrows the depletion region, allowing carriers to pass through the barrier via quantum tunneling. Doping at the $n \approx 10^{19}$ cm^{-3} level is one of the critical thresholds for Ohmic behavior. For n-type ZnO, metals with low work functions such as Ti, Al, and facilitate the formation of ohmic

contacts. The chemical stability of the metal is also important. Surface conditions at the metal-semiconductor interface determine whether the contact is Ohmic or Schottky in character by affecting the barrier height. Processes such as plasma cleaning and reducing surface roughness improve Ohmic behavior.

The design of ohmic contacts depends on many factors, such as the working function of the metal, the doping level of the semiconductor, surface cleanliness, and process conditions. Mo and W doping in ZnO-based thin films significantly improves ohmic behavior (Nogueira et al., 2023; Zhang et al., 2010).

2.4 XRD (X-Ray Diffraction)

In 1895, Wilhelm Roentgen obtained light beam by scattering high-energy electrons into a metal target. He could not understand the nature of these rays and he called them "X-Ray" (Röntgen, 1896).

The wavelength of X-Ray is between 0.1 nm - 0.001 nm and also 1000 times shorter than the wavelength of visible light. Their energy is therefore 1000 times greater than those of visible light.

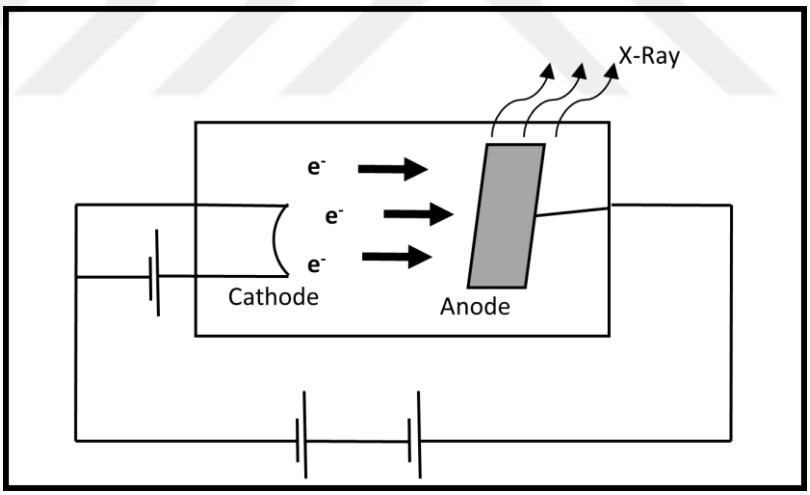

Figure 2.11. Illustration of an X-Ray tube (Öztel, 2019).

The Figure 2.11 above illustrates an X-ray source schematically. Electrons freely accelerate from the cathode toward the anode tungsten target when it is heated. The potential difference between the anode and cathode is what causes this motion. The electrons can travel at a speed of 0.1c thanks to this energy.

An X-ray that is perpendicular to the traveling electrons is produced when the electrons hit the target (Röntgen, 1896).

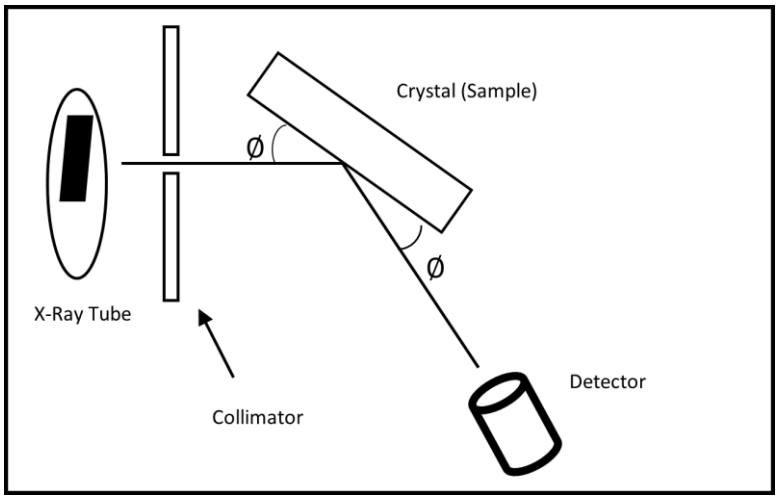

Figure 2.12. Schematic of X-Ray spectrometer (Öztel et al., 2024).

The light from X-ray spectroscopy is corrected by the collimator before being directed toward the crystal sample. A detector is then used to measure the intensity of the reflected light, as seen in Figure 2.12. By rotating the sample or adjusting the detector's angle, a spectrum can be acquired. This spectrum describes the structure of the crystal (Röntgen, 1896).

2.5 Fourier Transform Infrared Spectrometry (FTIR)

Transmittance and absorption spectra in the ultraviolet (UV) to near-infrared spectrum can be measured with spectrometers based on monochromators and slit systems. On the other hand, they are ineffective in the mid and far-infrared regions. Fourier transform infrared spectroscopy is more effective and appropriate in these areas. Furthermore, Fourier transform spectrometry generates precise and unambiguous data due to its fast output speed (Sardela, 2014).

Molecular vibrations, rotations, and wavenumbers generally engage with photon energy in the infrared region. The material's atomic structure depends on this. For this reason, Fourier transform infrared spectroscopy (FTIR) is a very beneficial technique for comprehending the structural characteristics of materials.Michelson-Morley experiment forms the basis of FTIR. This phenomenon can be clearly seen in Figure 2.13.

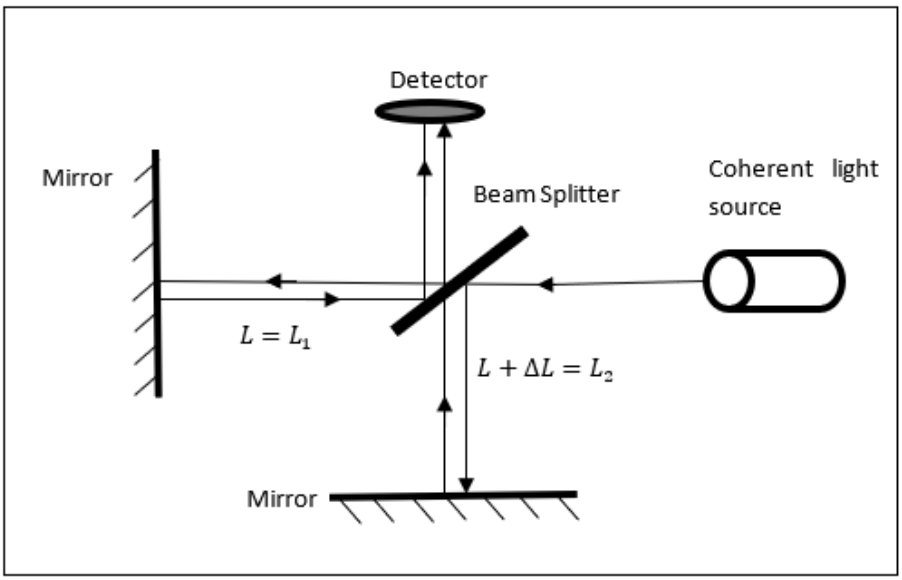

Figure 2.13. A Michelson-Morley interferometer (Öztel et al., 2024).

2.6 I-V Characteristics of a Diode

The current–voltage (I–V) characteristics of diodes are the fundamental electrical signature that shows how a p–n junction or metal–semiconductor (Schottky) structure performs carrier transport under non-equilibrium conditions. The forward bias current in an ideal p–n diode is given by the Shockley diode equation:

$$I = I_s[\exp(qV/nkT) - 1] \tag{2.22}$$

where $I\ S\ I_S$ is the saturation current, q q is the elementary charge, $k\ T$ is the thermal energy kT, and n n is the ideality factor (Neamen, 2002).

The exponential increase in current at low forward voltages occurs when the barrier decreases with external voltage, leading to the majority carrier injection and diffusion becoming dominant; in this region, the slope is determined by the ideality factor, where n≈1 indicates diffusion-controlled transport and n≈2 indicates recombination-controlled transport in the space-charge region (Neamen, 2002)As the voltage increases, the effect of the diode series resistance becomes more pronounced and the I–V curve deviates from the ideal exponential form and approaches a more linear appearance; therefore, when extracting the actual diode parameters, the series resistance and ideality factor are evaluated together (Cheung & Cheung, 1986). The series resistance and ideality factor are evaluated jointly

when extracting the actual diode parameters because the effect of the diode series resistance becomes more noticeable as the voltage increases and the I-V curve deviates from the ideal exponential form and approaches a more linear appearance (Cheung & Cheung, 1986).

In reverse bias, the current in an ideal p–n diode saturates around Is; in practice, the reverse current may increase, albeit weakly, depending on the voltage due to defect/interface states in the depletion region, thermal generation–recombination processes, and surface leakages(Neamen, 2002)

The diode enters the breakdown area, which is utilized functionally, particularly in regulation elements like Zener diodes, when the reverse voltage surpasses a crucial threshold due to Zener tunneling or avalanche propagation mechanisms (Neamen, 2002).

In summary, the diode I–V characteristic is read through the exponential conduction in the forward direction, deviations due to series resistance, leakage/saturation behavior in the reverse direction, and breakdown voltage; quantitative analysis of this curve plays a central role in determining the physical quality and transport mechanisms of both p–n junction and Schottky diodes by enabling the extraction of device parameters such as saturation current, ideality factor, series resistance, and barrier height (Aldemir et al., 2017).

2.7 Ideality Factor of a Diode

The diode ideality factor (n) is a fundamental parameter that quantifies the extent to which the current-voltage (I–V) behavior of a p–n junction or Schottky diode deviates from the ideal Shockley diode equation and provides direct information about the physical mechanisms that dominate carrier transport. In the ideal case, the forward current is described by the following equation,

$$I = I_0[\exp(qV/nkT) - 1] \tag{2.23}$$

where n = 1 indicates that the current is mostly determined by diffusion (intra-region carrier injection), while a value of n ≈ 2 corresponds to a situation where recombination (Shockley-Read-Hall recombination) dominates in the space charge region (Nicholls, 2021). In practice, n is usually greater than 1; the main reasons for this are defect/interface states at the metal-semiconductor interface,

barrier inhomogeneities due to band bending, series resistance effect and additional transport channels that occur at high injection conditions (Kaufmann et al., 2021).

The n value is also regarded as an indicator of the interface quality and the device fabrication process because, in Schottky diodes specifically, an increase in the ideality factor is linked to an increase in the interface state density and a deviation in the effective barrier height (Mallem et al., 2023). The ideality factor is usually derived from the slope of the forward semi-logarithmic I–V curve; however, when series resistance is significant, it is more reliably determined together with n and Rs using the Cheung–Cheung functions or Norde-type approximations (Cheung & Cheung, 1986). Consequently, the ideality factor is an indispensable quantity for diagnosing the current transport mechanism in diodes, evaluating interface defects, and optimizing fabrication parameters.

2.8 Structure and Properties of ZnO

Because of its broad band gap, excellent chemical stability, high exciton binding energy, and ease of fabrication, zinc oxide, or ZnO, is a popular material among Group II–VI compound semiconductors in both basic science and practical technology. ZnO has substantial absorption in the ultraviolet area and high optical transmittance in the visible range, with a direct band gap of roughly 3.2–3.37 eV at ambient temperature (Özgür et al., 2005). Because of this characteristic, ZnO has become a strategic material, especially in transparent electronic components, LED structures, UV photodetectors, and transparent conductive oxide (TCO) applications (Özgür et al., 2005). ZnO is useful for optoelectronic applications because of its high exciton binding energy of about 60 meV, which allows excitonic radiation to be preserved even at room temperature (Özgür et al., 2005).

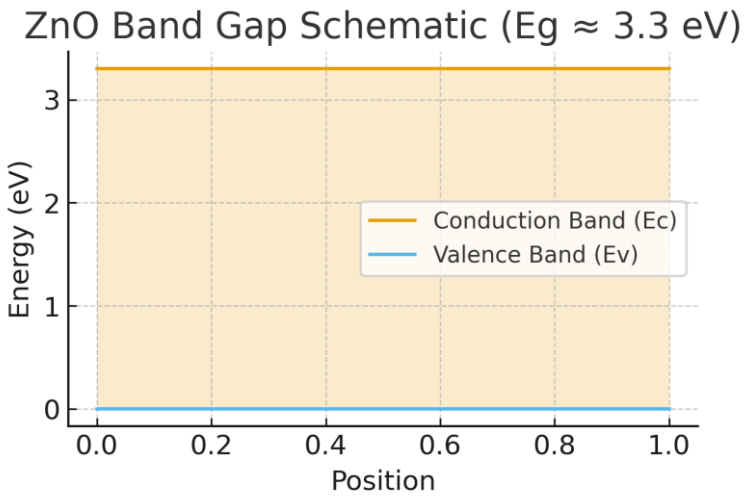

Figure 2.14. Illustration of the band gap of ZnO.

The Figure 2.14 showing the band gap of ZnO shows a direct band width of approximately 3.3 eV between the valence band (Ev) and the conduction band (Ec). This direct band structure allows ZnO to exhibit strong absorption in the UV region and maintain high transmittance in the visible region. Thanks to its wide band gap, free carriers can only be excited by high-energy photons, making ZnO preferred for UV photodetectors, UV LEDs, and transparent electronic components. The energy difference shown in the diagram also provides a fundamental reference for understanding the effects of dopants such as Mo and W on the band structure, as these dopants can contribute additional carriers to the conduction band, significantly affecting band occupancy and optical transitions.

Tetrahedral coordination of Zn and O atoms characterizes ZnO's hexagonal wurtzite crystal structure under normal circumstances. Significant electrical and mechanical effects result from the wurtzite crystal structure's polarity, especially in the direction parallel to the c-axis. This polarity causes directional growth in one-dimensional ZnO nanostructures, variations in surface energies, and chemically distinct behavior of Zn and O-terminated surfaces (Sood et al., 2025). The main cause of ZnO's piezoelectric characteristics is also this polar configuration. In this regard, ZnO provides notable benefits in applications including piezoelectric generators, flexible sensors, and surface acoustic wave (SAW) devices.

The defect chemistry of ZnO also largely determines the functional properties of the material. Oxygen vacancies (V_o) and zinc interstitial sites (Zn_i) are considered to be among the main reasons for the natural n-type conductivity of ZnO

(Özgür et al., 2005). The intermediate energy levels created by these defects directly affect the material's electrical conductivity, photoluminescence performance, carrier mobility, and optical absorption behavior. Deep-level emissions, in particular, are an important optical indicator that provides indirect information about the defect profile of ZnO. Reducing deep-level defects plays a critical role in producing high-quality ZnO films, especially for transparent conductive oxide applications (Huber et al., 2019).

The conductivity of ZnO can vary significantly depends on the conditions, defect density, and doping. According to Koç (2021), the film production methods (sol-gel, spray pyrolysis, sputtering, hydrothermal method, etc.) and the oxygen partial pressure can be used. Parameters such as film density, grain size, surface roughness, and defect distribution can be optimized in films depending on the solution chemistry and heat treatment profile. For example, it is an excellent technique for metal dopants such as Molybden and Tungsten due to the homogeneous dopant distribution (Bancheva-Koleva et al., 2024).

ZnO's optical and electrical performance is largely dependent on its geometrical characteristics. Higher crystallinity and better electrical conductivity can result from texture orientations found in thin films, especially those parallel to the (002) plane (Mary et al., 2017). The most significant microstructural factors influencing carrier mobility are the size and distribution of grain boundaries. Larger grains promote electron transport, whereas smaller grains decrease mobility because of more scattering points. Grain size and defect density both affect optical transmittance; larger defect density causes more scattering in the visible spectrum, which raises optical losses.

From an engineering standpoint, doping is one of the best methods for regulating ZnO's characteristics. In the ZnO structure, lower transition metal dopants like Mo and W usually substitute higher valence ions (Mo^{+}, W^{+}) for the Zn^{2+} ion, adding extra electrons and raising the free carrier density (Ganesh et al., 2022; Jalal et al., 2024). For transparent conductive oxide applications, Mo and W dopants are therefore very effective at increasing ZnO's conductivity. According to Bancheva-Koleva et al. (2024), Mo doping can result in a modest narrowing of the band and preserve good permeability without upsetting the crystal structure when employed at the right ratios.

According to reports, W doping enhances UV photodetector performance, especially by making carrier separation easier (Ganesh et al., 2022; Jalal et al., 2024) In sol-gel manufacturing, Mo and W dopants can also improve microstructural density and film texture. Nevertheless, it has also been documented in the literature that high dopant concentrations might have negative consequences such reduced carrier mobility, increased surface roughness, and crystal deterioration (Huber et al., 2019).

Considering all these contexts, the structural, optical, and electrical properties of ZnO are determined by a multidimensional mechanism shaped by the strong interaction between crystal structure, defect chemistry, fabrication method, and dopant type/level. Mo and W-doped ZnO thin films produced by the sol-gel method provide a suitable platform for experimental control of these interactions. Therefore, understanding the structural and physical properties of ZnO is directly relevant to the thesis topic in terms of determining accurate doping strategies and provides the necessary theoretical basis for interpreting experimental characterization results.

2.9 Doping Mechanisms in ZnO

Doping mechanisms in ZnO are based on the increase in carrier density generated by ions added to the lattice by exogenous dopants, beyond innate defects such as oxygen vacancies (V_o) and zinc intercalations (Zn_i), which determine the material's natural n-type conductivity. Donor-type dopants (Al^{3+}, Ga^{3+}, Mo^{6+}, W^{6+}, etc.) generally replace the Zn^{2+} ion, transferring excess electrons to the conduction band, thereby increasing the free electron concentration (Özgür et al., 2005). The placement of these highly valenced ions in the lattice can alter band occupancy and optical transitions via the Burstein–Moss effect, while also affecting crystal strain and grain boundary properties (Huber et al., 2019)Although acceptor-type dopants (such as N, P, and As) can theoretically create p-type conductivity, it is quite difficult to obtain stable p-type ZnO due to self-compensating defects in ZnO (Sood et al., 2025). Therefore, doping mechanisms in ZnO research are mostly discussed through the conductivity-enhancing effects of donor dopants and their relationship with structural and optical properties.

2.10 Effects of Mo and W Doping on Optical and Electrical Properties

Transparent conducting oxides (TCOs), UV photodetectors, and thin-film electronics depend on how Mo and W doping affects the optical and electrical characteristics of ZnO thin films. In its pure condition, ZnO, a wide-bandgap, direct-transition semiconductor, has high visual transmittance and relatively high resistance; from an engineering standpoint, an acceptable compromise between these two properties can be obtained with the right doping. When high-valent transition metals like Mo and W are added to the ZnO lattice as Mo^{+} or W^{+} instead of Zn^{2+}, more electrons are added to the conduction band, which raises the free carrier density and greatly enhances electrical conductivity (Mekki & Tabet, 2014; Wu et al., 2015). These dopants also affect the lattice parameters, bond order, and defect structure, leading to shifts in the optical band gap and absorption–transmittance curves in the visible/UV regions.

When looking at the effect of Mo doping on electrical properties, many studies have reported a decrease in resistivity of one order of magnitude or more at optimum dopant concentrations. For example, Wu and co-workers produced Mo-doped ZnO (MZO) thin films by DC magnetron sputtering, achieving the lowest resistivity of ~9.2×10^{-4} Ω·cm and showed that mobility and carrier density changed sensitively with dopant concentration (Wu et al., 2015). Swapna and co-workers, on the other hand, investigated the structural, electrical, and optical properties of Mo-doped ZnO films together and reported that conductivity improved with increasing Mo content, but carrier mobility decreased due to microstructural distortions at high dopant levels (Swapna et al., 2013). Similar trends are observed in solution growth techniques such as sol–gel, spray pyrolysis, or SILAR; While film resistance decreases as the Mo concentration increases up to a certain threshold, when this threshold is exceeded, deterioration in total conductivity occurs due to effects such as grain boundary growth and second phase formation (Bancheva-Koleva et al., 2024; Radha et al., 2016). This is also critical for 2% and 4% Mo-doped ZnO films, requiring separate evaluation of both carrier density and mobility for each concentration.

Optically, Mo doping can have a bidirectional effect on the band gap and visible transmittance. Bancheva-Koleva and colleagues achieved optical transmittance between 77% and 84% in the visible region in ZnO films doped with

0–2 mol% Mo produced by spray pyrolysis, and reported that the band gap varies slightly with the doping amount (Bancheva-Koleva et al., 2024). While some studies observed a blue shift in the band gap (Burstein–Moss effect) with Mo doping, others reported a slight narrowing of the band due to intermediate energy levels and lattice distortions (Mekki & Tabet, 2014; Radha et al., 2016). This difference depends on the production method, annealing conditions, crystallinity of the films, and the actual chemical position of Mo within the ZnO lattice. However, the general trend is that in well-crystallized ZnO films, Mo doping can modulate band-edge absorption in the UV region, depending on the dopant concentration, while largely maintaining high transmittance in the visible region (Altuntepe & Erkan, 2025). In this context, the effect of Mo doping on optical properties should be evaluated not only through band gap shift but also through free carrier absorption and scattering mechanisms.

The effect of W doping on optical and electrical properties is based on a physical basis like that of Mo, but its combination of high conductivity and high transmittance is particularly prominent in the literature. Zhang and colleagues achieved optical transmittance and low resistivity values above 80% on glass substrates in W-doped ZnO (ZnO:W) thin films produced by DC magnetron sputtering, suggesting these films as candidates for transparent conductive films (Zhang et al., 2010).

Similarly, Adachi and colleagues, growing pure and W-doped ZnO films using pulsed laser deposition, showed that carrier density increases with increasing W content, but electron mobility decreases at very high doping rates (Adachi et al., 2014).

These results indicate that W doping should be kept within an optimum range, as with Mo; otherwise, conductivity saturation or decline may occur due to microstructural distortions and increased scattering. A recent study by Mei and colleagues also emphasized that W doping significantly improves the electrical properties of ZnO thin films, and that this doping strategy is widely used in many applications such as TCO, solar cells, and UV detectors (Mei et al., 2024).

In terms of optical properties, W doping can finely tune the band gap and UV optical response while largely preserving the transparency of ZnO in the visible region. Pan and colleagues achieved over 80% optical transmittance in the visible region in 1 wt.% W-doped ZnO films prepared by the PLD method, and reported

that the band gap was maintained in the range of 3.31–3.36 eV (Pan et al., 2022). In their comprehensive study of metal-doped ZnO systems, Huber and colleagues reported that the effective band gap can be as high as 4.10 eV when some W-doped ZnO films exhibit amorphous properties, which can be advantageous for short-wavelength optical applications (Huber et al., 2019).

These studies demonstrate that W doping has an effect on the band structure that is sensitive to both the crystal structure and the degree of amorphization. From an optical transition engineering perspective, W doping can also improve band alignment by slightly shifting the UV absorption edge, enabling ZnO-based photodetectors and perovskite solar cells to function as electron transport layers (Gantumur et al., 2024)

When the effects of Mo and W dopants on optical and electrical properties are considered together, it can be said that both dopants are powerful tools for making ZnO a transparent conductive film and a candidate for high-performance optoelectronic components. While Mo doping is primarily important for conductivity and optical bandgap tuning, W doping has been found to be particularly effective in improving parameters such as photoresponsivity, dark current, and detector stability in UV photodetector structures (Jalal et al., 2024). Comparing 2% W-doped ZnO thin films produced via the sol–gel method with these trends reported in the literature will provide a clearer picture of the dopant concentration-property relationship in terms of both optical bandgap and I–V characteristics. In conclusion, Mo and W doping can lower resistivity, adjust the bandgap, and enhance device performance while maintaining high optical transmittance in ZnO. However, the optimum doping ratio must be carefully determined based on the fabrication method and targeted application.

2.11 Fundamentals of the Sol–Gel Method and Coating Process

The sol–gel method is a wet chemistry-based process that allows the synthesis of inorganic ceramic and glass-based materials at relatively low temperatures with high purity and homogeneity. This method begins with the dissolution of molecular precursors such as metal alkoxides or metal salts in suitable solvents and continues with the formation of a three-dimensional network structure of a "gel" phase, linked by metal–oxygen–metal (M–O–M) bridges, through sequential hydrolysis and condensation reactions (Hench & West, 1990)

The system begins as a homogenous sol phase and eventually changes into a dense network structure made up of polymeric chains or colloidal particles. The microstructure of the resultant thin film, and therefore its optical and electrical properties, are shaped throughout this transformation by processes like increased viscosity, improved network connectivity, and porosity evolution (Danks et al., 2016). Precursor solution preparation, hydrolysis and condensation, gelation, aging, drying, and frequently a heat treatment step (calcination or densification) are the fundamental stages of the sol-gel process, which includes sol preparation, gel formation, and heat treatment as a sequential process flow.

The creation of M–O–M bridges as a result of the hydrolysis reactions of metal alkoxides with water and the condensation reactions of these hydrolysis products with one another is the basis of the sol–gel process. Numerous factors, including the water/alkoxide molar ratio, solvent type, pH, catalyst (acid/base) use, and temperature, affect the kinetics of hydrolysis–condensation (Hench & West, 1990; Periyasamy et al., 2020). A three-dimensional, denser network structure forms at high hydrolysis rates, whereas more linear or slightly branched polymeric chains form at low hydrolysis rates. Over time, the sol phase gelatinizes into a macroscopic "gel" phase due to the connectivity of these polymer chains or colloidal particles. Gel formation alters the rheological behavior of the system; viscosity increases rapidly, and the porous structure carried by the network structure determines whether the thin film will be porous or compact during subsequent drying and densification stages (Brinker et al., 1992).

During gel aging, the network structure is re-dissolved, weak bonds are strengthened, and internal stresses are relieved. During the drying phase, the removal of the liquid phase from the gel results in bulk and prominence due to capillary forces. The resulting tensile stresses can cause cracking, especially in monolithic structures; in thin film geometry, the films themselves and surface roughness effects (Hench & West, 1990). While small film growth facilitates the management of drying stresses in thin films, rapid solvent evaporation and uncontrolled thermal gradients can still lead to crack formation; therefore, the residual temperature and drying conditions must be carefully selected. Subsequent heat treatment (usually between 300 and 600 °C) removes organic residues, densifies, and crystalline phase development begins. Especially for films developed by the sol-gel method for ZnO and similar metal oxides, heat treatment temperature

and time have a strong influence on crystal size, preferences and hence optical/electrical properties (Gallagher & Ring, 1989).

Using a variety of coating processes, the solution produced by the sol-gel procedure can be applied as a thin layer on the substrate surface. The three most popular coating methods are spray, spin, and dip coating (Brinker et al., 1991; Butt, 2022). The substrate is submerged in a solution at a set rate during dip coating, and it is then removed at a controlled rate. A liquid film of a particular thickness forms on the substrate surface depending on the drawing speed, sol viscosity, surface tension, and environmental factors. Solvent evaporation and subsequent condensation processes cause this liquid film to change into a gel layer (Brinker et al., 1991). The most important benefit of dip coating is the ease with which multilayer films can be created and even substrates with complicated geometries may be coated rather uniformly. In spin coating, the substrate is rapidly rotated as the solution is sprayed onto the surface.

A thin, reasonably homogeneous film is left behind as the solution spreads away from the surface due to centrifugal force and viscous movement. In optical and electrical applications requiring great surface smoothness, especially at submicron thickness, spin coating is recommended (Butt, 2022; Gallagher & Ring, 1989). Spray coating is a technique that allows for large-area coating by atomizing and spraying sol-gel solutions onto the substrate; it is particularly useful for large-surface substrates and industrial-scale production (Periyasamy et al., 2020).

The broad tunability of layer thickness and microstructure is one of the major benefits of sol-gel-based coating techniques. Film thickness can be adjusted from nanometers to a few micrometers by varying the drawing speed, spin speed, sol viscosity, solids concentration, and multiple coating–heat treatment cycles (Brinker et al., 1992; Puetz & Aegerter, 2004). The degree of hydrolysis/condensation, sol composition, and heat treatment parameters can all be used to modify the porosity and refractive index of films produced with sol–gel coatings, offering significant flexibility for optical coatings, antireflective films, and sensor surfaces (Figueira, 2020; Ulrich, 1990). Additionally, both inorganic and organic–organic hybrid systems are made possible by sol–gel chemistry, which allows for the creation of multifunctional coatings (such as hybrid films that offer both corrosion resistance and optical functionality) as well as substrate-compatible mechanical and thermal expansion coefficients (Danks et al., 2016; Figueira, 2020).

As a result, the sol-gel process stands out as a potent and adaptable platform for the creation of sophisticated functional coatings, sensor surfaces, and optoelectronic components in addition to traditional ceramic films.

As a result, the sol-gel technique and related coating procedures entail a series of chemical and physical transformations that go from the molecular level to the macroscopic film. The final structural, optical, and electrical characteristics of the thin film are determined by each stage of this transformation, including hydrolysis, condensation, gelation, drying, densification, and coating parameters. Therefore, a thorough grasp of not only the precursor chemistry employed but also the basic concepts of the sol–gel process and the coating dynamics is crucial for interpreting the results in investigations on the manufacture of ZnO and Mo/W-doped ZnO thin films using the sol–gel method.

3. MATERIALS AND METHODS

1% and 4% W doped films, and 2% and 4% Mo doped ZnO films were produced at Nanotechnology Laboratory in Istanbul University (IU). The production steps will be given in the next sections.

3.1 Preparation of Solution

Solutions and gels are two forms of matter that have long been known to exist naturally. They include a variety of materials, such as ink and clay, as well as many substances such as vitreous humor, blood, serum, and milk. Solutions and gels have long been a focus of scientific interest. The earliest laboratory-prepared solutions were synthesized with gold by Faraday in 1853, and they remain stable today (Pierre, 2020).

As for gels, with the exception of some naturally occurring silica gels, their synthesis was only achieved in the 19th century. Ebelmen produced the first silica gel in 1846, and Cossa synthesized the first alumina gel in 1870 (Pierre, 2020). For a long time, solutions were of only scientific interest. However, their extremely high specific fields made them increasingly attractive in the field of catalysis. Following Matijevic's work in England in the early 1960s on the production of colloidal particles of controlled size and shape using clay and nuclear fuel oxides, materials for more technical use were produced. Since the 1970s, an increasing number of scientific publications have been published in the field of gels and inorganic colloids. These high-tech materials have become increasingly interesting, and their applications have expanded, so much so that some have already been commercialized. New sol-gel processes can now meet, at least to some extent, the current need for new and improved products. High-purity nanoscale powders, thin films, nuclear fuels, electronic components and semiconductors, and magnetic materials can now be produced using sol-gel techniques. Sol-gel techniques are a very useful method when the reproducible production of homogeneous complex materials is required. In fact, sol-gel techniques are often considered the path to "better materials through chemistry." However, fundamental aspects of physics are also very important and should not be neglected. These include, in particular, DLVO theory, the percolation approach to gelation, and, more generally, the

"ultrastructure" design of any mechanical or magnetic property (i.e., at the scale of very small clusters of atoms) (Pierre, 2020).

The sol-gel approach is a very useful and quick technology that provides controllability, reproducibility, and an easy-to-manufacture, reasonably priced procedure. In technical terms, a solution is a stable suspension of nanoparticles, or colloidal particles, in a liquid. The particles have dense, porous, or polymeric structures and can be crystalline or amorphous. Moreover, they may consist of collections of sub colloidal chemical units. In contrast, a gel is made up of a continuous liquid phase (wet gel) that is surrounded and supported by a porous, three-dimensionally continuous solid network. Covalent bonding between sol-gel particles causes gelation, or gel formation, in the majority of sol-gel systems used to synthesize oxide materials. When additional bonds, such hydrogen bonds or van der Waals forces, are present, gel formation is reversible. The structure of a gel network depends largely on the size and shape of the sol particles (Hesemann et al., 2015).

For a solution to exist, the solid particles, denser than the surrounding liquid, must be small enough in size to ensure that the forces responsible for dispersion are greater than the force of gravity. Furthermore, these particles must contain a macroscopically significant number of atoms. In practice, the particles in a colloidal sol must have a size between 2 nm and 0.2 μm, corresponding to 10^3 to 10^9 atoms per particle. The solvent used to stably disperse the colloidal particles of a solution is usually either pure water or a solution of water. However, other solvents, such as alcohol, can also be used (Pierre, 2020).

A gel is a porous, three-dimensionally interconnected solid network that expands stably throughout a liquid medium, limited only by the size of the container. If this solid network is composed of colloidal sol particles, the gel is said to be colloidal. If the solid network consists of sub colloidal chemical units, the gel is polymeric. As defined by Flory, a polymer is a group of molecules whose structure can be formed by "the repetition of one or more fundamental units." Inorganic solutions and gels exist in a wide variety. The nature of gels depends on the coexistence of the solid network and the liquid medium. The liquid is located between the solid network forming the gel. It does not flow spontaneously and is in thermodynamic equilibrium with the solid network. If the liquid consists mostly of water and this aqueous phase is largely present, the corresponding gel is called a

hydrogel. A hydrogel is a soft material that can be easily cut with a knife. Conversely, if the liquid phase consists primarily of alcohol, the gel is called an alcogel. Finally, if most of the liquid is removed, the resulting brittle solid is called either a xerogel or an aerogel, depending on the drying method. These may also be simply called dry gels (Pierre, 2020).

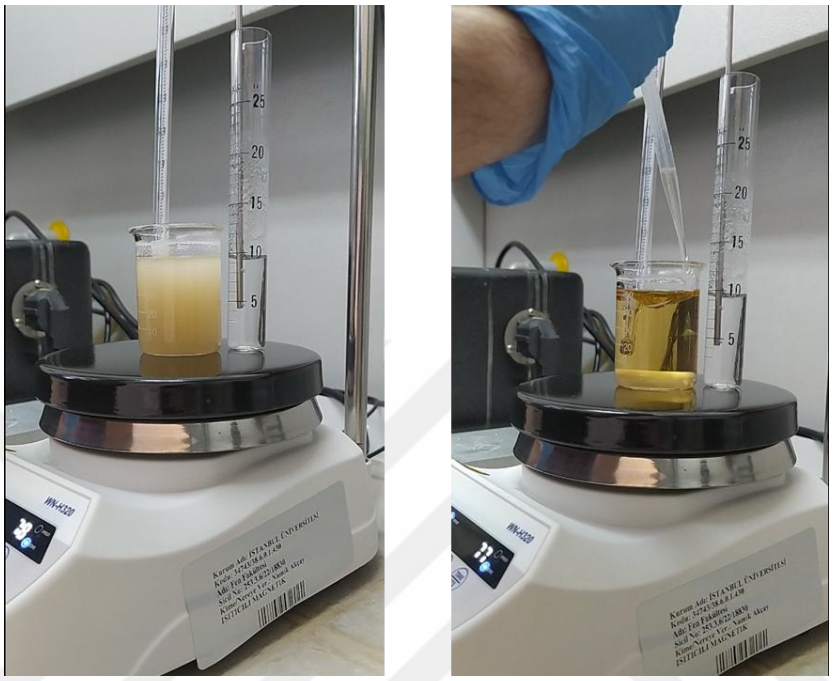

Figure 3.1. Before and after photos after catalyst was used for Mo nanoparticles.

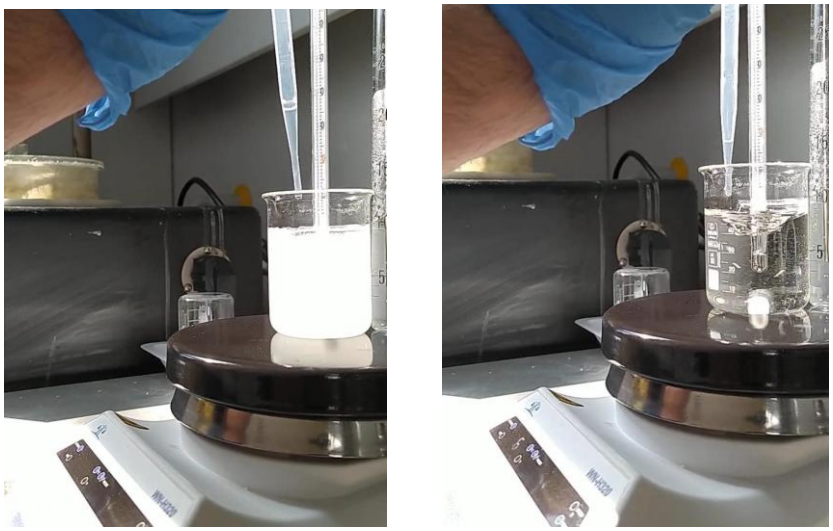

Figure 3.2. Before and after photos after catalyst was used for W nanoparticles.

Sufficiently rapid cooling prevents a thermodynamically favorable crystalline structure, and rapid, nearly irreversible reactions are the cause of amorphous network structures in sol-gel materials. Therefore, sol-gel materials are metastable solids formed by kinetically controlled reactions from molecular

precursors that form the building blocks of subsequent materials. The implication is that all reaction parameters, including precursor properties, have a decisive influence on the structure and, consequently, the properties of the sol-gel material (Hesemann et al., 2015).

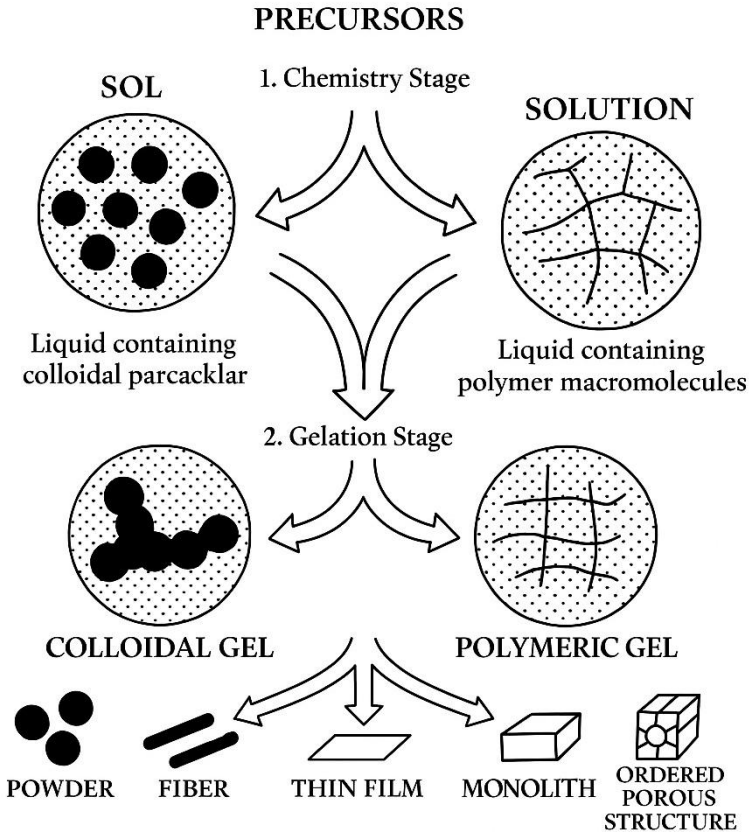

Figure 3.3. Schematic diagram of the production process of Sol-Gel. This sketch was adopted from Oztel (2024).

It is also possible to synthesize small ceramic pieces using a completely monolithic process that prevents fracture after simple sintering. Furthermore, pore size can be controlled by supercritical drying or the use of surface-active agents (surfactants). Figure 3.3 roughly illustrates how these coating approaches relate to the sol-gel procedure and how they are essentially categorized. Many different routes and many unexplored intermediate paths exist (Pierre, 2020).

In this thesis, the sol-gel technique was used to produce pure ZnO and Mo-W doped ZnO nanostructures. The production of the nanostructures was carried out in the Nanotechnology Research Laboratory of the Physics Department of the Faculty of Science at Istanbul University.

In first step of experiment Tungsten, Molybdenum, Scandium has been chosen as dopant after necessary comparisons had been investigated from the

literature. Zinc Acetate is used as solvent in this experiment. For dopants following materials have been used: Tungsten Hexacarbonyl, Molybdenum Hexacarbonyl, Zinc acetate dihydrate as a zinc source (99.999%, trace metals basis).

Synthesis of Pure ZnO Nanostructure

3.292 g of zinc acetate dihydrate was weighed on a precision scale and added to 50 ml of 2-methoxyethanol to achieve a molar ratio of 0.3 M. The solution was then stirred on a magnetic stirrer for 15 minutes. Meanwhile, the temperature of the magnetic stirrer was adjusted to maintain a solution temperature of 80 °C. When the temperature reached 80 °C after 15 minutes, approximately 0.9 ml of ethanolamine was added to achieve a molar ratio of 1:1 and stirred at 400 rpm for 90 minutes. The solution, which was white until the stabilizer was added, became transparent when the stabilizer was added. At the end of the process, the heater was turned off, and the solution was stirred until it reached room temperature. Finally, the solution was transferred to a suitable storage container.

Synthesis of 2% and 4% Mo doped ZnO nanostructure

4.215 g of zinc acetate dihydrate and 0.072 g for 2% then, 0,144 g for 4% molybdenum hexacarbonyl were measured and combined with 50 ml of 2-methoxyethanol to create a molar ratio of 0.3 M. The mixture was subsequently stirred in a magnetic stirrer for 15 minutes. Simultaneously, the temperature of the magnetic stirrer was set to keep the solution's temperature at 80 °C. When the temperature reached 80 °C after 15 minutes, approximately 0.9 ml of ethanolamine was added to achieve a molar ratio of 1:1 and stirred at 400 rpm for 90 minutes. The solution, which was white until the stabilizer was added, became transparent when the stabilizer was added. At the end of the process, the heater was turned off, and the prepared solution was stirred until it reached room temperature. Finally, the solution was transferred to a suitable storage container.

Synthesis of 2% and 4% W doped ZnO nanostructure

4.214 g of zinc acetate dihydrate and 0.025 g for 1% W and 4.302g zinc acetate dihydrate and 0.1 g for % W Tungsten Hexacarbonyl were measured and combined with 50 ml of 2-methoxyethanol to create a molar ratio of 0.3 M. The mixture was subsequently stirred in a magnetic stirrer for 15 minutes. Simultaneously, the temperature of the magnetic stirrer was set to keep the

solution's temperature at 80 °C. When the temperature reached 80 °C after 15 minutes, approximately 0.9 ml of ethanolamine was added to achieve a molar ratio of 1:1 and stirred at 400 rpm for 90 minutes. The solution, which was white until the stabilizer was added, became transparent when the stabilizer was added. At the end of the process, the heater was turned off, and the prepared solution was stirred until it reached room temperature. Finally, the solution was transferred to a suitable storage container.

3.2 Preparation of Heterojunctions

Nanostructures prepared by the sol-gel method were spin-coated onto boron (B)-doped Si (111) (p-Si) (MTI Corporation (USA). The thickness of the Si crystal was 0.65–0.7 mm, and the resistivity was 5–10 Ω.cm. The silicon wafer was cut into 1 cm x 1 cm dimensions to prepare for the coating process. The surfaces were cleaned with a dry air pump to remove any remaining dust grains. The surfaces of the cut p-Si were first cleaned of the dirt layer that might have formed during cutting using a special dust-free and non-scratching napkin and acetone. Then, for precise surface cleaning, the p-Si was cleaned in an ISOLAB ultrasonic bath with alcohol and then acetone for 2 minutes each. The p-Si surface was then kept in a 1:10 hydrofluoric acid (HF, 42%) solution for 5 minutes to remove the oxide layer on it. It was then placed in distilled water and placed in a suitable storage container (Öztel et al., 2024).

To create ohmic back contacts, the prepared p-Sis were coated with aluminum (Al) (99.999%) on their back surfaces with a thickness of approximately 175 nm using appropriate masks (Fang et al., 2007; Ocaya et al., 2023). The coating process was carried out under a vacuum of ~10–6 mbar with an Edwards Model 6E (Edwards, UK) thermal evaporator device.

The front surfaces of the p-Si nanoparticles, for which the back contact point was created, were spin-coated with the prepared nanoparticles. The coating procedure utilized ISOLAB adjustable micropipettes, applying 20 µL of solution drop by drop for every layer. The speed of rotation during the coating process was observed at 2000 rpm. Intermediate heating was utilized between each layer. The aim of this intermediate heating was to eliminate leftover liquid solution from the prior coating and to enhance the adhesion of the previous layer to the surface before the application of the second layer. This intermediary heating was performed at

around 250 °C under atmospheric pressure for a duration of 2 min. The coating process was carried out three times, leading to a total of 3 layers applied. The fabricated heterojunctions were subsequently baked (Oztel, 2024).

The firing process was carried out in a closed furnace of the MAGMATHERM MT 1305-E4 brand and model at 450 °C for 1 hour, increasing the temperature by 4 °C per minute. The purpose of this annealing process was to purify the organic compounds that could not be completely removed during the intermediate heating and to obtain a better crystal structure (Yousefi et al., 2011). Finally, the thermal evaporator process was repeated for the upper surface ohmic contacts with Al using a suitable mask, again with a coating thickness of 175 nm (Yıldız et al., 2023).

4. RESULTS

In this section, graphs and analyses of XRD, FTIR, and I–V and the ideality factor calculations performed to reveal the structural, vibrational, and electrical properties of molybdenum and tungsten-doped ZnO thin films will be presented in detail. XRD data will be used to evaluate the crystalline phases, grain sizes of each film, peak positions, and crystal size changes of the films; potential stresses and orientational differences in the lattice structure caused by doping ratios will be interpreted. FTIR spectra will be examined to determine the fundamental vibrational bands of Zn–O bonding and the effects of dopants on the bonding environment.

These analyses aim to provide complementary information about the location of the dopant elements within the material. Current–voltage curves obtained as part of I–V characterization will be used to evaluate the rectification characteristics of the structure and electrical carrier transport mechanisms. Furthermore, ideality factors calculated from forward-bias data will enable the investigation of diode interface quality and deflection mechanisms.

All graphs and numerical analyses presented in this section will systematically demonstrate the changes in film properties depending on doping ratios.

4.1 XRD Results of Doped ZnO Films

The XRD patterns of 2-4% Molybdenum doped films and 1% Tungsten doped films were analyzed. XRD patterns and peaks analyzed via the software which is commonly used for the analyze International Center for Diffraction. XRD data taken by Rigaku Multiflex X-Ray Diffractometer in Bolu Abant Izzet Baysal University (BAIBU), which is shown in Figure 4.1.

Figure 4.1. Rigaku Multiflex XRD Diffractometer in BAIBU, Bolu, Turkey.

The XRD graph of a 2% Mo-doped ZnO thin film is presented in Figure 4.2. The peaks seen in the graph indicate that the film retains its hexagonal wurtzite structure and that the Mo addition does not cause a significant phase transformation in the crystal structure. Details of the measurements are given in the Figure 4.2, Figure 4.3 and Figure 4.4. All films scanned within the range of 20 to 80 degree.

The XRD graph of a 4% Mo-doped ZnO thin film is shown in Figure. The location and intensity of the peaks in the graph indicate that the film retains its wurtzite ZnO crystal structure despite the high Mo content. The changes in peak widths and intensities depending on the Mo doping are clearly visible in the figure.

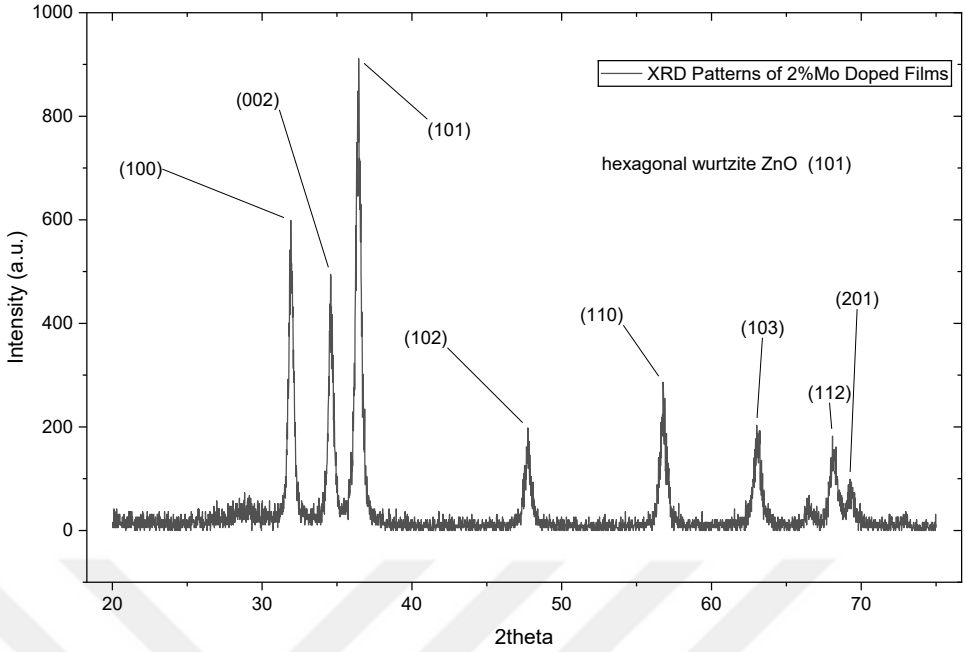

Figure 4.2. XRD spectra of 2% Mo doped ZnO thin film.

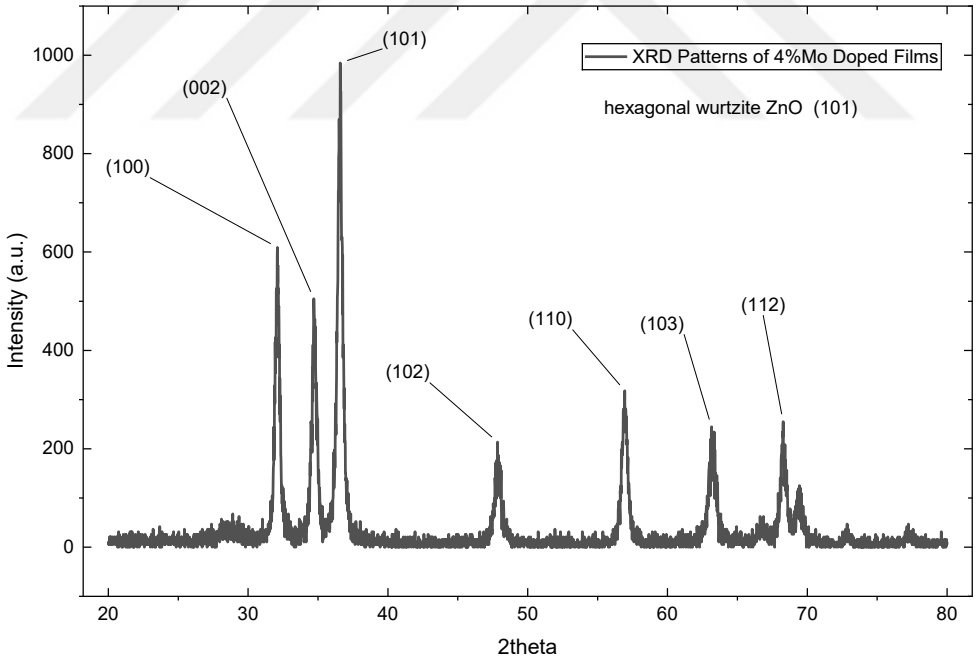

Figure 4.3. XRD spectra of 4% Mo doped ZnO thin film.

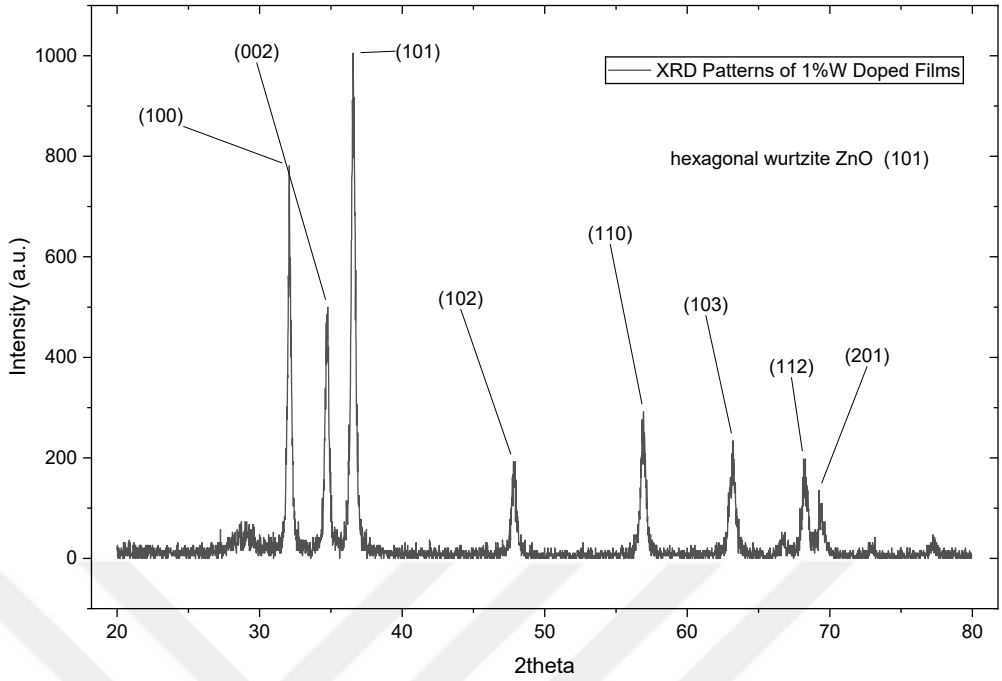

Figure 4.4. XRD spectra of 1% W doped ZnO thin film.

The XRD graph of a 1% W-doped ZnO thin film is presented Figure 4.4. The location of the peaks in the graph indicates that the film maintains the wurtzite ZnO crystal structure and that the low doping level does not significantly degrade the lattice integrity.

Table 4.1. Grain size of each films.

	2 theta	**Grain Size (nm)**	**c-parameter(Å)**	**a-parameter (Å)**
2% Mo	36.416	22.32	5.206	3.241
4% Mo	36.571	22.08	5.165	3.232
1% W	36.564	24.35	5.156	3.232

The crystallite size (P) and lattice strain can be found to be Scherer's formula Equation 4.1 (Zsigmondy & Scherrer, 1912).

$$P = \frac{0.9\lambda}{\beta Cos(\theta)} \quad \text{Scherer's Formula} \tag{4.1}$$

Calculated values are listed in the Table 4.1. Then calculations shows that by increasing the doping concentration of the Molybdenum the grain sizes slightly decrease. Also a and c parameter decreased aswell.

4.2 I-V Characteristics of ZnO Thin Films

The I–V characteristics of a 2% Mo-doped ZnO thin film are shown in Figure 4.5. As can be seen from the graph, the diode exhibits a “front region” with low current in the forward direction up to approximately +3 V; after this voltage, the current increases sharply, exhibiting diode-like rectification behavior.

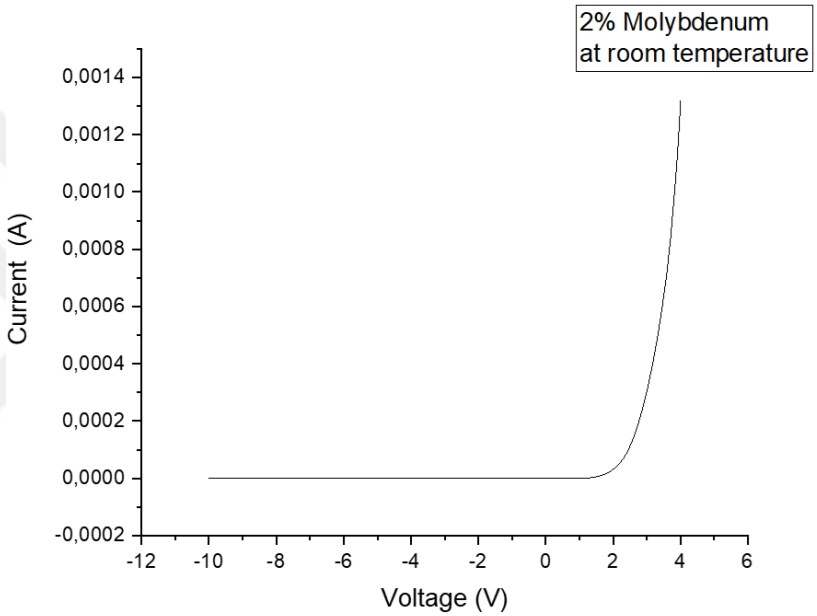

Figure 4.5. 2% Mo doped ZnO/p-Si films I-V measurement results at room temperature.

This pronounced forward rectification trend supports the preservation of diode behavior in ZnO at low Mo doping levels. Donor-doped ZnO films have been reported in the literature to exhibit similar exponential conduction transitions Therefore, it can be said that the 2% Mo-doped film offers a stable diode character in terms of rectification ratio and current transport mechanism.

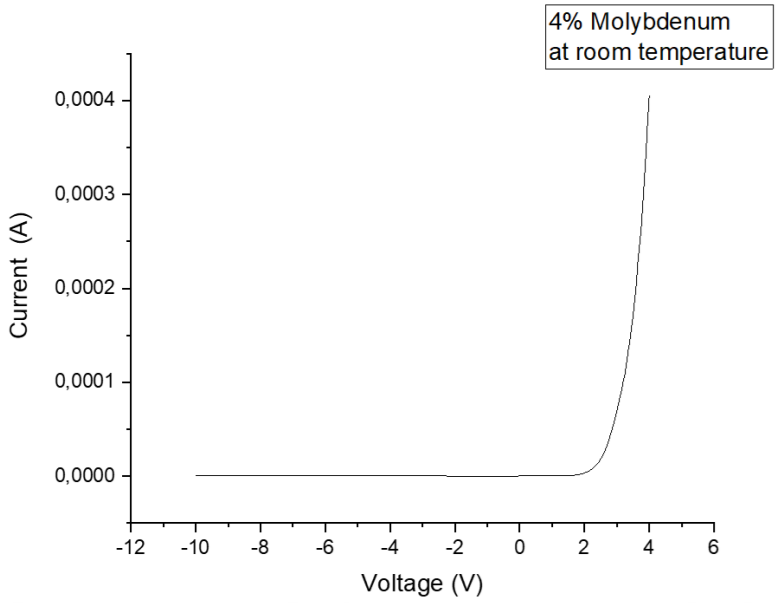

Figure 4.6. 4% Mo doped ZnO/p-Si films I-V measurement results at room temperature.

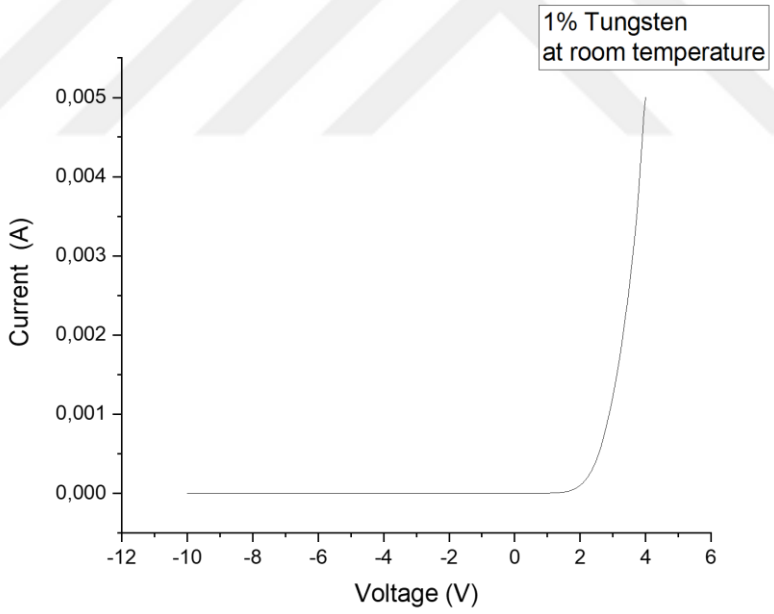

Figure 4.7. 1% W doped ZnO/p-Si films I-V measurement results at room temperature.

4.3 Ideality Factor

The obtained ideality factor values (n = 4.90, 7.97, 6.18, and 6.21) show significant deviations from the ideal medium behavior. The ideal case of n is widened in the range of 1–2, while higher values generally indicate frequency

imperfections, inhomogeneities of filter gaps, series resistance effects, pressure values, and pressure at reconnection centers.

Table 4.2. Serial resistance and ideality values for each films.

	Serial Resistance (R_s)	**Ideality Factor**
2% Mo	1,16E+6 Ohm/sq	4.90
4% Mo	8,78E+5 Ohm/sq	7.97
1% W	1.15E+7 Ohm/sq	6.18
4% W	1,31E+7 Ohm/sq	6.21

4.4 Fourier Transform Infrared Spectroscopy (FTIR) Results

The identity of the functional groups, molecular interactions, and chemical structure of the W- and Mo- doped thin films which was figured out with Fourier Transform Infrared Spectroscopy (FTIR). The obtained results are shown in the Figure 4.8, Figure 4.9, and Figure 4.10 for 2% and 4% Mo-doped films and 1% W-doped films respectively. FTIR results was taken via Perkin Elmer Spectrum Two FTIR-ATR Spectrophotometer in Inorganic Research Laboratory in BAIBU.

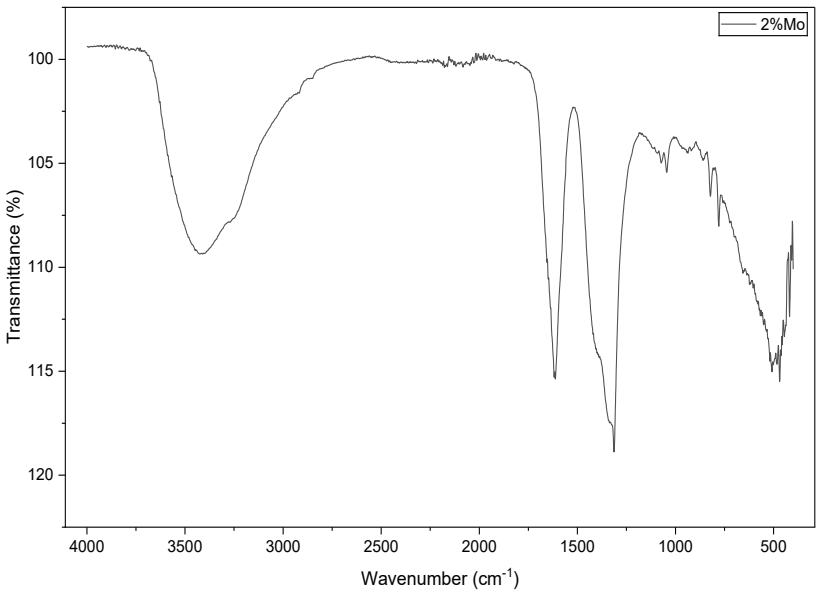

Figure 4.8. The FTIR analysis of 2% Mo-doped ZnO thin film

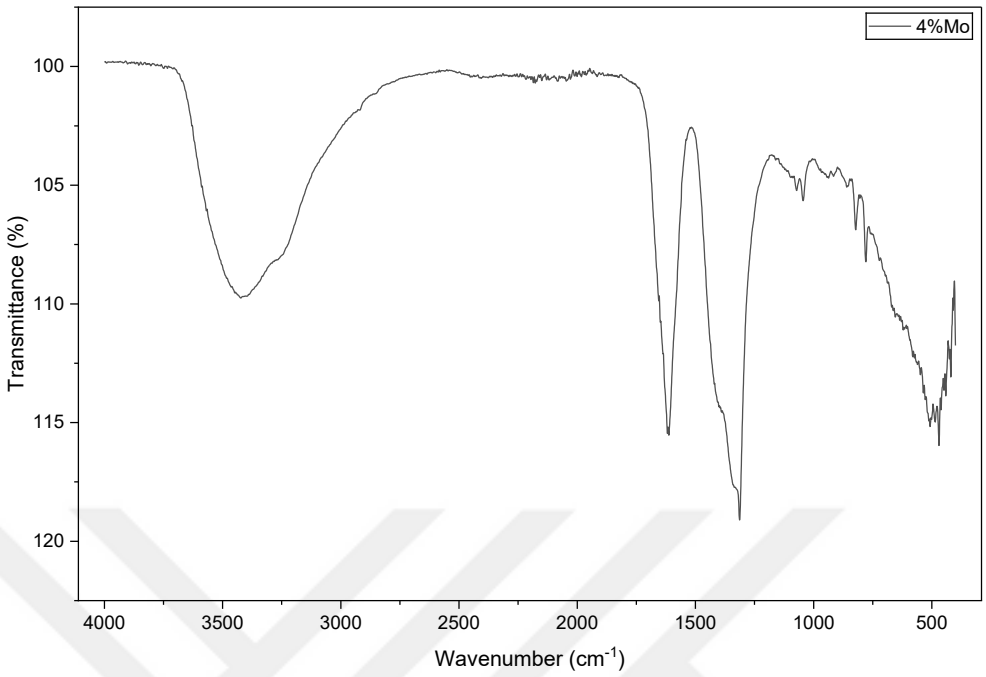

Figure 4.9. The FTIR analysis of 4% Mo-doped ZnO thin film

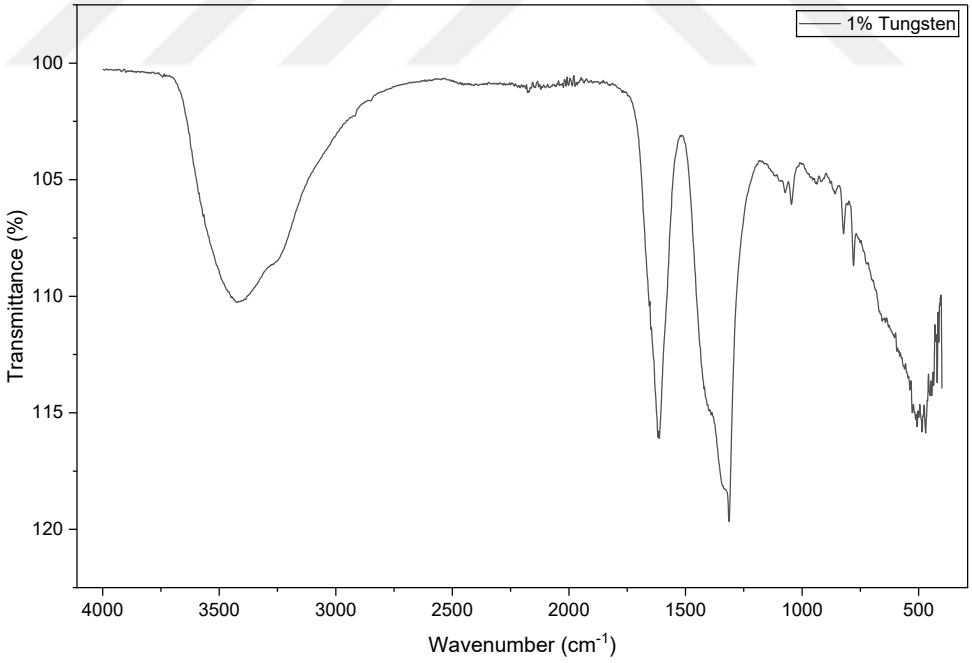

Figure 4.10. The FTIR analysis of 1% W-doped ZnO thin film

The synthesized zinc oxide (ZnO) nanoparticles were examined by FTIR spectroscopy to identify the characteristic functional groups associated with the

prepared material. The spectrum showed distinct absorption bands at 3437.8, 2925.8, 1595.8, 1383.7, 1355.5, 1118.1, 1005.3, 863.3, 776.8, 700.6, and 575.9 cm^{-1}. The band at 575.9 cm^{-1} is attributed to the metal–oxygen stretching vibration (Zn–O) of ZnO. The peak at 1005.3 cm^{-1} can be assigned to C–N stretching of primary amines or, alternatively, to C–O stretching of primary alcohols. The bands observed at 1118.1, 1355.5, and 1383.7 cm^{-1} are associated with in-plane bending/vibrational modes of primary and secondary alcohol groups. The absorption at 1595.8 cm^{-1} is related to vibrational modes of aromatic nitro compounds and alkyl groups. In addition, the bands at 2925.8 and 3437.8 cm^{-1} correspond to the stretching vibrations of hydroxyl-containing compounds.

5. DISCUSSION

5.1 XRD Analysis

According to obtained XRD patterns of each films, only the 1% W-doped film was evaluated in this study because literature reports that free carrier scattering and lattice distortions become more pronounced as W doping increases, negatively affecting the smooth carrier transport necessary for diode behavior (Pan et al., 2022). Therefore, it is known that diode properties deteriorate at high doping levels and that optimum performance is achieved with a low W content. The peak widths and intensities in the XRD pattern at the 1% doping level confirm that the film maintains its single-phase structure and has a suitable crystallization quality for measurements.

A slight decrease in grain size (22.32 → 22.08 nm) occurred as the Mo doping increased from 2% to 4%. This decrease suggests that doping slightly inhibits crystal growth at higher rates, resulting in more grain boundaries. This behavior has also been observed in the literature, where the doping causes lattice distortion and narrows the diffusion pathway (Huber et al., 2019). In this case, crystal quality may decrease slightly, and grain size may decrease as the doping increases.

However, the grain size obtained in the 1% W-doped film is larger than the other films, at 24.35 nm. This suggests that low W doping either inhibits crystal growth less or directs crystal play more efficiently. In other words, a low doping rate of 1% is below the critical destructive threshold and relatively preserves grain growth. Various studies have reported that such low doping rates can both maintain crystal quality and increase carrier density (Pan et al., 2022).

Declining trend is observed in the c-parameter values. This reduction illustrates the stress placed on the crystal lattice by the dopant ions substituting the Zn^{2+} ion. For instance, Mo^{6+} or W^{6+} ions might possess different ionic radii in comparison to the Zn^{2+} ion, potentially leading to either a shrinking or an expansion of the lattice parameters. The literature describes these lattice strain induced by dopants (Mekki & Tabet, 2014). Therefore, the noted reduction in the c-parameter as the dopant ratio rises indicates that the dopant ions, found in greater concentrations, are applying pressure on the crystal lattice or forming a more compact structure

Taking these comments together, the larger grain size and relatively smaller c-parameter decrease achieved with low-level W doping (1%) may reflect the carrier density-enhancing effect of the doping, combined with higher crystal quality. On the other hand, smaller grain sizes and more pronounced c-parameter reductions were observed with higher Mo doping amounts (especially 4%), indicating that the doping limits grain growth through its effect on the crystal structure. In this study, it would be appropriate to discuss how these values correlate with carrier mobility, optical bandgap changes, and diode behavior.

It is clearly seen that XRD results of obtained films are in hexagonal wurtzite ZnO phase. Mainly obtained peaks are $2\theta \approx 31.7°$, 34.4° ve 36.2° and they are in (100), (002) and (101) crystal planes respectively. These peak locations and their relative distributions are in good agreement with the standard JCPDS No: 36-1451 reference chart reported for ZnO (Özgür et al., 2005).

In addition, other diffraction peaks observed at higher angles and coupled to planes such as (102), (110), (103), (112)/(201) originate from high-index planes belonging to the wurtzite structure of ZnO. Despite the Mo and W doping, the absence of characteristic peaks belonging to secondary phases such as MoO_3 or WO_3 suggests that the dopants are incorporated into the ZnO crystal lattice in a substitutional manner. However, the broadening and density changes observed in some peaks, especially with increasing Mo doping, can be attributed to dopant-induced microstrain and crystal defect increase, as also stated in the literature (Huber et al., 2019; Mekki & Tabet, 2014). These results demonstrate that XRD data reliably reveal both phase purity and the effect of doping on the crystal structure.

5.2 Electrical Properties

This exponential increase can be attributed to the activation of majority carrier injection due to the increase in carriers created near the conduction band of the Mo doping. In the reverse bias, the current remains approximately constant down to the −10 V region, indicating the formation of a well-insulated interface with low leakage current. The I–V plot of a 4% Mo-doped ZnO thin film is shown in Figure 4.6. It is observed that the current increases rapidly after approximately +3 V in the forward direction, indicating that the film maintains diode-like rectification behavior. However, it is noteworthy that the forward current is lower

at the 4% doping level than at 2% Mo, indicating that the high Mo content limits current transport due to crystalline distortion and carrier scattering. In the reverse direction, the current remains low down to −10 V, indicating that the film still provides a stable interface in terms of leakage current. It has been reported in the literature that high Mo doping can weaken the conduction properties of ZnO (Pan et al., 2022).

The I–V plot of a 1% W-doped ZnO thin film is presented in Figure 4.7. The rapid rise in forward current around +3 V indicates that the film exhibits a pronounced diode rectification behavior. In the reverse bias, the current remains very low over a wide voltage range, indicating limited leakage current and good interface quality. Due to the low doping ratio, the film has a more ordered crystal structure and more efficient carrier flow than highly doped samples, consistent with literature findings that lower W doping levels provide better diode performance (Pan et al., 2022).

If we were to make an assessment in terms of the ideality factor, it is stated that most circuit ideality factors, especially for ZnO, Mo-doped ZnO, and W-doped ZnO-based Schottky methods, are in the range of 1.5–4, while higher values indicate increased distortion or defects. For example, Huber et al. (2019) reported that in metal-doped ZnO structures, dopant insulation barrier inhomogeneity becomes pronounced and can exceed 5 in this case. Similarly, Cheung and Cheung (1986) emphasized that high n values generally promote series resistance effects and local barrier changes. Pan et al. (2022) show that when the doping ratio increases in W-doped ZnO films, crystal defects become abundant and the diode deviates from the ideal. Considering these literature data, the relatively high ideality factor of 7.97 in the 4% Mo-doped film in this study indicates that increasing Mo doping causes distortion in the crystal structure, creating more traps and scattering centers at the interface. The finding of n = 4.90 in the 2% Mo-doped film indicates that the defect effect decreases relatively as the doping amount decreases. The values around n ≈ 6 obtained in the W-doped films suggest that the interface quality is not entirely ideal despite the low doping level, but that Mo provides more balanced transport compared to the high doping rate. The high ideality factor in all structures generally indicates that current transport is not

limited to diffusion; instead, mechanisms such as trap filling, recombination, interface disorder, and local barrier changes dominate.

5.3 Optical Properties

FTIR data for Mo- and W-doped ZnO films demonstrate typical oxide thin-film behavior, with the characteristic Zn–O vibration band in the 400 - 4000 cm^{-1} range and the effects of the doping on the lattice clearly visible. All three spectra show a significant increase in absorption at low wavenumbers (approximately 400–600 cm^{-1}); this region corresponds to the fundamental Zn–O stretching vibration mode of ZnO and has been reported in the literature for ZnO in the range of 420–550 cm^{-1} (Handore et al., 2014).

The more pronounced increase in absorption intensity in the low-frequency region in the 1% W-doped film (~24.35 nm grain size) compared to the Mo-doped films suggests that the W doping causes less distortion in the Zn–O lattice and better preserves crystal integrity. This finding is consistent with studies reporting that W doping creates a more stable bond interaction with ZnO at low levels (Pan et al., 2022).

In the 2% Mo-doped film, the absorption intensity in the Zn–O vibration region is lower than in the W-doped film, but the spectrum is smooth and continuous. This indicates that Mo has embedded in the lattice but does not cause significant phase separation. Slight absorbance changes in the middle region, around 1400–1600 cm^{-1}, may be related to the presence of hydroxyl (–OH) groups on the Zn-O surface; this is common in oxide films produced by the sol–gel method (Brinker et al., 1992).

In the 4% Mo-doped film, the absorption slope in the low-frequency region is more irregular compared to the Mo 2% and W1% films, and slope changes are observed around the Zn-O band. This suggests that higher Mo doping levels cause greater distortion of the Zn-O lattice, i.e., increased local bond disorder and crystal strain. This observation is consistent with the smaller crystallite sizes (22.08 nm) obtained in the XRD analysis and is supported by literature studies indicating that high Mo doping induces strain in the ZnO lattice (Mekki & Tabet, 2014).

When all spectra are examined, it can be said that the overall FTIR behavior indicates a single-phase oxide structure; as the doping amount increases, the Zn-O vibration band is slightly suppressed and lattice distortion increases, while lower W

doping results both provide a more pronounced Zn-O band and better crystal quality. When this assessment is considered together with the XRD and I–V analyses, the FTIR results appear to support the structural and electrical finding.

It does not appear that a new “completely different” functional group has emerged; however, as the dopant ratio/type increases, the band intensities and profiles change significantly, particularly in the 1600–1300 and 1200–800 cm^{-1} regions; there are also minor differences in the Zn–O (700–500 cm^{-1}) band.

6. CONCLUSION

In this thesis, ZnO thin films doped with Mo (2% and 4%) and W (1% and 4%) were successfully synthesized using the sol–gel method, and their structural, optical, and electrical properties were investigated comprehensively. XRD and FTIR analyses revealed that the dopants were evenly distributed within the film matrix thanks to the chemical homogeneity offered by the sol–gel process. XRD results showed that the hexagonal wurtzite ZnO phase was preserved in all films; however, as the doping ratio increased, crystalline distortion and crystallite size were reduced, particularly in films containing Mo. The decrease in the c-parameter value and the pronounced peak broadening at 4% Mo doping confirm the increased stretching effect of the dopant on the ZnO lattice. FTIR spectra also revealed that the Zn–O vibrational modes were preserved in all samples; however, with higher Mo doping, vibrational band irregularities increased. The W-doped film, on the other hand, exhibited higher crystal integrity and a more pronounced Zn–O band, supporting the positive effect of lower doping.

Electrical measurements, particularly I–V characteristics, confirmed that the films exhibited diode-like behavior; however, the high ideality factor values indicated that carrier transport was limited by interface defects, barrier inhomogeneity, and recombination processes. The increase in ideality factor as Mo doping increased supports this interpretation. The more stable electrical performance of the W-doped film compared to the others was attributed to better preservation of crystal integrity.

Beyond these basic conclusions, the study's overall findings offer significant insights into the behavior of doped ZnO systems and the intricate interactions between carrier transport pathways, dopant concentration, and microstructural evolution. Producing repeatable and compositionally homogeneous films is a benefit of the sol-gel process, which enables fine control of precursor chemistry at the molecular level.

The increased distortion observed in Mo-doped ZnO films is likely related to the substitution of Mo ions into Mo^{6+} sites at Zn^{2+} sites, and the smaller ionic radius and higher oxidation state creating significant strain in the lattice. In addition the behavior of W-doped films, particularly at lower doping levels, suggests that W ions cause a more balanced distortion of the lattice. The lower structural disorder

compared to Mo suggests that W^{6+} ions create fewer compensation defects at low concentrations or exhibit more harmonious interactions with the local bonding environment. In this respect, the difference between Mo and W demonstrates that the dopant type is as critical as the dopant amount.

Electrical characterization results complement these structural findings. The relatively high ideality factors—especially in Mo-doped films—indicate that current transport cannot be explained solely by thermionic emission, but rather by local barrier heights, interface states, and defect-centered transport mechanisms. The further increase in the ideality factor in the highly Mo-doped film confirms that the increased defect density limits charge carriers to diffusion and recombination processes. In contrast, the relatively more stable ideality factor in the W-doped film indicates a more uniform barrier height distribution and lower trap density.

In conclusion, this study provides novel insights into the behavior of Mo- and W-doped ZnO thin films and illuminates the fundamental principles of how dopant-induced changes occur in semiconductor oxides. The findings clearly demonstrate that successful device performance is achieved not only through dopant addition, but also through precise optimization of the dopant type, amount, lattice interaction, and effects on defect formation. This comprehensive assessment further demonstrates the crucial role of dopant engineering in the development of ZnO-based electronic and optoelectronic systems.

Overall, the results indicate that low dopant levels improve both structural integrity and electrical performance in ZnO thin films; high Mo doping levels reduce crystal quality; and the optimal dopant level for W doping is critical for diode behavior. The findings obtained in this thesis clearly demonstrate that dopant engineering plays a critical role in determining the performance of ZnO-based electronic and optoelectronic devices.

7. REFERENCES

Adachi, Y., Saito, N., Hashiguchi, M., Sakaguchi, I., Suzuki, T., Ohashi, N., & Hishita, S. (2014). Electrical and optical properties of W-doped ZnO films grownon (11\bar {2} 0) sapphire substrates using pulsed laser deposition. *Journal of the Ceramic Society of Japan*, *122*(1430), 908-913.

Ahmad, M. R., Ansari, A. A., Dhayal, M., & Lv, R. (2025). Bandgap engineering of ZnO nanomaterials for enhanced electrochemical and photocatalytic efficiency. *Renewable and Sustainable Energy Reviews*, *219*, 115767.

Aldemir, D. A., Kökce, A., & Özdemir, A. F. (2017). The comparison of the methods used for determining of Schottky diode parameters in a wide temperature range. *Sakarya University Journal of Science*, *21*(6), 1286-1292.

Alsaad, A., Al-Bataineh, Q. M., Ahmad, A., Albataineh, Z., & Telfah, A. (2020). Optical band gap and refractive index dispersion parameters of boron-doped ZnO thin films: A novel derived mathematical model from the experimental transmission spectra. *Optik*, *211*, 164641.

Altuntepe, A., & Erkan, S. (2025). Enhancing optoelectronic performance: Structural and optical properties of. *Eurasian Journal of Science Engineering and Technology*, *6*(1), 36-40. https://doi.org/10.55696/ejset.1604813

Amakali, T., Daniel, L. S., Uahengo, V., Dzade, N. Y., & de Leeuw, N. H. (2020). Structural and Optical Properties of ZnO Thin Films Prepared by Molecular Precursor and Sol–Gel Methods. *Crystals*, *10*(2), 132. https://www.mdpi.com/2073-4352/10/2/132

Bancheva-Koleva, P., Zhelev, V., Petkov, P., & Petkova, T. (2024). Molybdenum-doped ZnO thin films obtained by spray pyrolysis. *Materials*, *17*(9), 2164.

Bokov, D., Turki Jalil, A., Chupradit, S., Suksatan, W., Javed Ansari, M., Shewael, I. H., Valiev, G. H., & Kianfar, E. (2021). Nanomaterial by sol‐gel method: synthesis and application. *Advances in materials science and engineering*, *2021*(1), 5102014.

Brinker, C. J., Frye, G., Hurd, A., & Ashley, C. (1991). Fundamentals of sol-gel dip coating. *Thin solid films*, *201*(1), 97-108.

Brinker, C. J., Hurd, A. J., Schunk, P. R., Frye, G. C., & Ashley, C. S. (1992). Review of sol-gel thin film formation. *Journal of Non-Crystalline Solids*, *147-148*, 424-436. https://doi.org/https://doi.org/10.1016/S0022-3093(05)80653-2

Brinker, C. J., & Scherer, G. W. (1990). *Sol-gel science: the physics and chemistry of sol-gel processing*. Gulf Professional Publishing.

Butt, M. A. (2022). Thin-film coating methods: a successful marriage of high-quality and cost-effectiveness—a brief exploration. *Coatings*, *12*(8), 1115.

Chen, N., Ramzan, I., Li, S., & Carmalt, C. J. (2024). Synthesis and Characterization of Optically Transparent and Electrically Conductive Mo-Doped ZnO, F-Doped ZnO, and Mo/F-Codoped ZnO Thin Films via Aerosol-Assisted Chemical Vapor Deposition. *Crystal Growth & Design*, *24*(24), 10256-10266.

Chen, T.-H., & Jian, B.-L. (2016). Optical and electronic properties of Mo: ZnO thin films deposited using RF magnetron sputtering with different process parameters. *Optical and Quantum Electronics*, *48*(2), 77.

Cheung, S., & Cheung, N. (1986). Extraction of Schottky diode parameters from forward current—Voltage characteristics. *Applied Physics Letters*, *49*, 85-87. https://doi.org/10.1063/1.97359

Colinge, J.-P., & Colinge, C. A. (2002). *Physics of semiconductor devices*. Springer.

Danks, A. E., Hall, S. R., & Schnepp, Z. (2016). The evolution of 'sol–gel'chemistry as a technique for materials synthesis. *Materials Horizons*, *3*(2), 91-112.

Fang, Z.-Q., Claflin, B., Look, D. C., Kerr, L. L., & Li, X. (2007). Electron and hole traps in N-doped ZnO grown on p-type Si by metalorganic chemical vapor deposition. *Journal of applied physics*, *102*(2).

Figueira, R. B. (2020). Hybrid sol–gel coatings for corrosion mitigation: A critical review. *Polymers*, *12*(3), 689.

Gallagher, D., & Ring, T. (1989). Sol--Gel Processing of Ceramic Films. *Chimia*, *43*(10), 298-304.

Ganesh, V., Hussien, M. S., Shaik, U. P., Ade, R., Mohammed, M. I., AlAbdulaal, T. H., Zahran, H. Y., Yahia, I. S., & Abdel-wahab, M. S. (2022). Impact of Mo-Doping on the structural, optical, and electrocatalytic degradation of ZnO nanoparticles: Novel approach. *Crystals*, *12*(9), 1239.

Gantumur, M., Hossain, M. I., Shahiduzzaman, M., Tamang, A., Rafij, J. H., Shahinuzzaman, M., Thi Cam Tu, H., Nakano, M., Karakawa, M., & Ohdaira, K. (2024). Tungsten-doped ZnO as an electron transport layer for perovskite solar cells: enhancing efficiency and stability. *ACS Applied Materials & Interfaces*, *16*(28), 36255-36271.

Handore, K., Bhavsar, S., Horne, A., Chhattise, P., Mohite, K., Ambekar, J., Pande, N., & Chabukswar, V. (2014). Novel Green Route of Synthesis of ZnO Nanoparticles by Using Natural Biodegradable Polymer and Its Application as a Catalyst for Oxidation of Aldehydes. *Journal of Macromolecular Science Part A Pure and Applied Chemistry*, *51*, 941. https://doi.org/10.1080/10601325.2014.967078

Hench, L. L., & West, J. K. (1990). The sol-gel process. *Chemical reviews*, *90*(1), 33-72.

Hesemann, P., Viau, L., & Vioux, A. (2015). The Sol-Gel Handbook - Synthesis, Characterization, and Applications: Synthesis, Characterization and Applications, 3-Volume Set. In (pp. 487-518). https://doi.org/10.1002/9783527670819.ch16

Huber, S., Mardare, C. C., Kleber, C., & Hassel, A. W. (2019). Structural, electrical, and optical effects of metal doping on ZnO thin films. *physica status solidi (a)*, *216*(12), 1800942.

Jalal, R., Ozel, K., Atilgan, A., & Yildiz, A. (2024). UV photodetectors based on W-doped ZnO thin films. *Nanotechnology*, *35*(26), 265705.

Jiamprasertboon, A., Dixon, S. C., Sathasivam, S., Powell, M. J., Lu, Y., Siritanon, T., & Carmalt, C. J. (2019). Low-Cost One-Step Fabrication of Highly Conductive ZnO:Cl Transparent Thin Films with Tunable Photocatalytic Properties via Aerosol-Assisted Chemical Vapor Deposition. *ACS Appl Electron Mater*, *1*(8), 1408-1417. https://doi.org/10.1021/acsaelm.9b00190

Kaufmann, I. R., Zerey, O., Meyers, T., Reker, J., Vidor, F., & Hilleringmann, U. (2021). A Study about Schottky Barrier Height and Ideality Factor in Thin Film Transistors with Metal/Zinc Oxide Nanoparticles Structures Aiming Flexible Electronics Application. *Nanomaterials (Basel)*, *11*(5). https://doi.org/10.3390/nano11051188

Kim, S.-H., Kim, K.-K., Park, S.-J., & Seong, T.-Y. (2005). Thermally Stable and Low Resistance Re/Ti/Au Ohmic Contacts to n ZnO. *Journal of the Electrochemical Society*, *152*(3), G169.

Koç, M. (2021). Ultrasonik sprey piroliz ile üretilen ZnO ince filmlerin alttaş sıcaklıklarının yapısal ve optik özelliklerine etkisi. *Süleyman Demirel University Faculty of Arts and Science Journal of Science*, *16*(1), 169-178.

Liu, Y., Li, Y., & Zeng, H. (2013). ZnO ‐ based transparent conductive thin films: doping, performance, and processing. *Journal of Nanomaterials*, *2013*(1), 196521.

Mallem, S. P. R., Puneetha, P., Choi, Y., Baek, S. M., Lee, D.-Y., Im, K.-S., & An, S. J. (2023). Barrier Height, Ideality Factor and Role of Inhomogeneities at the AlGaN/GaN Interface in GaN Nanowire Wrap-Gate Transistor. *Nanomaterials*, *13*(24), 3159.

Mary, A. J. R., & Arumugam, S. (2017). Structural and optical studies of molarity based ZnO thin films. *Nano Hybrids and Composites*, *17*, 140-148.

Mattox, D. M. (2010). *Handbook of physical vapor deposition (PVD) processing*. William Andrew.

Mei, H., Wang, W., Zhao, J., Zhong, W., Qiu, M., Xu, J., Gao, K., Liu, G., Liang, J., & Gong, W. (2024). Effect of Bias Voltage on the Microstructure and Photoelectric Properties of W-Doped ZnO Films. *Nanomaterials*, *14*(24), 2050.

Mekki, A., & Tabet, N. (2014). Synthesis, Structural and Optical Properties of Mo-Doped ZnO Thin Films. *Acta Physica Polonica A*, *125*, 367-369. https://doi.org/10.12693/APhysPolA.125.367

Merghes, P., Ilia, G., Maranescu, B., Varan, N., & Simulescu, V. (2024). The sol–gel process, a green method used to obtain hybrid materials containing phosphorus and zirconium. *Gels*, *10*(10), 656.

Neamen, D. (2002). *Semiconductor Physics And Devices*. McGraw-Hill, Inc.

Ng, K. K., & Sze, S. M. (2007). *Physics of semiconductor devices*. Wiley-Interscience Hoboken, NJ.

Nicholls, J. R. (2021). Electron trapping effects in SiC Schottky diodes: Review and comment. *Microelectronics Reliability*, *127*, 114386. https://doi.org/https://doi.org/10.1016/j.microrel.2021.114386

Nogueira, G. L., Kumar, D., Zhang, S., Alves, N., & Kettle, J. (2023). Zero waste and biodegradable zinc oxide thin-film transistors for UV sensors and logic circuits. *IEEE Transactions on Electron Devices*, *70*(4), 1702-1709.

Ocaya, R. O., Al-Sehemi, A. G., Tataroğlu, A., Dere, A., Erol, I., Aksu, M., Al-Ghamdi, A. A., & Yakuphanoğlu, F. (2023). Effect of CuO doping on the performance of LaB6 interlayer films in Al/CuO: LaB6/p-Si/Al diodes. *Physica B: Condensed Matter*, *666*, 415111.

Oztel, H. O. (2024). *Ce KATKILI Zno/Si HETEROEKLEMİNİN ÜRETİMİ Ve ARA*

YÜZEYDE OLUŞAN KUSUR SEVİYELERİNİN İNCELENMESİ Istanbul University].

Özgür, Ü., Alivov, Y. I., Liu, C., Teke, A., Reshchikov, M. A., Doğan, S., Avrutin, V., Cho, S.-J., & Morkoç. (2005). A comprehensive review of ZnO materials and devices. *Journal of applied physics*, *98*(4).

Öztel, H. O., Akçay, N., & Algün, G. (2024). Deep-level transient spectroscopy analysis of interface defects in Ce: ZnO/p-Si heterostructures. *Journal of Materials Science: Materials in Electronics*, *35*(18), 1247.

Öztel, S. (2019). *Fabrication And Characterization of Doped Metal-Oxide Semiconductor Thin Film Gas Sensors* Bolu Abant Izzet Baysal University].

Pan, P.-C., Koo, H.-S., Chen, D.-X., & Chen, C.-M. (2022). Fabricating High-Conduction and High-Transparency Tungsten-Doped Zinc Oxide Films by Pulse Laser Deposition Technique. *Crystals*, *12*(8), 1032. https://www.mdpi.com/2073-4352/12/8/1032

Periyasamy, A. P., Venkataraman, M., Kremenakova, D., Militky, J., & Zhou, Y. (2020). Progress in sol-gel technology for the coatings of fabrics. *Materials*, *13*(8), 1838.

Piegari, A., & Flory, F. (2018). *Optical thin films and coatings: From materials to applications*. Woodhead Publishing.

Pierre, A. C. (2020). *Introduction to sol-gel processing*. Springer Nature.

Pierret, R. F. (1996). *Semiconductor device fundamentals*. Pearson Education India.

Puetz, J., & Aegerter, M. A. (2004). Dip Coating Technique. In M. A. Aegerter & M. Mennig (Eds.), *Sol-Gel Technologies for Glass Producers and Users* (pp. 37-48). Springer US. https://doi.org/10.1007/978-0-387-88953-5_3

Qiu, W. (2025). *The influence of Li-doping on the structural and optical characteristics of ZnO thin films*. https://doi.org/10.1117/12.3069780

Radha, R., Sakthivelu, A., & Raj, P. (2016). Synthesis and characterization of molybdenum doped ZnO thin films by SILAR deposition method. *Radha, R., Sakthivelu, A., & Pradhabhan, D.(2016). Synthesis and Characterization of Molybdenum Doped ZnO Thin Films by SILAR Deposition Method. IRA-International Journal of Applied Sciences (ISSN 2455-4499)*, *4*(1).

Röntgen, W. C. (1896). On a New Kind of Rays. *Science*, *3*(59), 227-231. https://doi.org/doi:10.1126/science.3.59.227

Sales Amalraj, A., Christina Joycee, S., & Natarajan, G. (2022). Investigation of the properties of tungsten doped ZnO thin films synthesised by SILAR method. *Materials Research Innovations*, *26*(5), 263-269.

Sardela, M. (2014). *Practical materials characterization*. Springer.

Shaw, A., Whittles, T. J., Mitrovic, I. Z., Jin, J. D., Wrench, J. S., Hesp, D., Dhanak, V. R., Chalker, P. R., & Hall, S. (2015, 14-18 Sept. 2015). Physical and electrical characterization of Mg-doped ZnO thin-film transistors. 2015 45th European Solid State Device Research Conference (ESSDERC),

Singh, J., Kumar, S., Alok, A., Upadhyay, S. K., Rawat, M., Tsang, D. C., Bolan, N., & Kim, K.-H. (2019). The potential of green synthesized zinc oxide nanoparticles as nutrient source for plant growth. *Journal of Cleaner Production*, *214*, 1061-1070.

Smith, D. L., & Hoffman, D. W. (1996). Thin ‐ film deposition: principles and practice. In: American Institute of Physics.

Sood, S., Kumar, P., Raina, I., Misra, M., Kaushal, S., Gaur, J., Kumar, S., & Singh, G. (2025). Enhancing Optoelectronic Performance Through Rare-Earth-Doped ZnO: Insights and Applications. Photonics,

Swapna, R., Ashok, M., Muralidharan, G., & Kumar, M. S. (2013). Microstructural, electrical and optical properties of ZnO: Mo thin films with various thickness by spray pyrolysis. *Journal of Analytical and Applied Pyrolysis*, *102*, 68-75.

Sygletou, M., Benedetti, S., di Bona, A., Canepa, M., & Bisio, F. (2022). Doping-dependent optical response of a hybrid transparent conductive oxide/plasmonic medium. *The Journal of Physical Chemistry C*, *126*(4), 1881-1889.

Sze, S. (1985). DEVICES,“. *Semiconductor Physics and technology*.

Tung, R. T. (2014). The physics and chemistry of the Schottky barrier height. *Applied Physics Reviews*, *1*(1).

Ulrich, D. R. (1990). Prospects for sol-gel processes. *Journal of Non-Crystalline Solids*, *121*(1-3), 465-479.

Vines, F., Iglesias-Juez, A., Fernandez-Garcia, M., & Illas, F. (2018). Understanding W doping in wurtzite ZnO. *The Journal of Physical Chemistry C*, *122*(33), 19082-19089.

Wasa, K., & Hayakawa, S. (1992). Handbook of sputter deposition technology.

Wu, M., Yu, S., Chen, G., He, L., Yang, L., & Zhang, W. (2015). Structural, optical, and electrical properties of Mo-doped ZnO thin films prepared by magnetron sputtering. *Applied surface science*, *324*, 791-796.

Xiu, F., Xu, J., Joshi, P., Bridges, C., & Paranthaman, P. (2016). ZnO Doping and Defect Engineering—A Review. *Springer Series in Materials Science*, *218*, 105-140. https://doi.org/10.1007/978-3-319-20331-7_4

Xu, L., Li, X., Chen, Y., & Xu, F. (2011). Structural and Optical Properties of ZnO Thin Films Prepared by Sol–Gel Method With Different Thickness. *Applied Surface Science - APPL SURF SCI*, *257*, 4031-4037. https://doi.org/10.1016/j.apsusc.2010.11.170

Yıldız, D. E., Kocyigit, A., & Yıldırım, M. (2023). Comparison of Al/TiO2/p-Si and Al/ZnO/p-Si photodetectors. *Optical Materials*, *145*, 114371.

Yousefi, M., Azimirad, R., Amiri, M., & Moshfegh, A. (2011). Effect of annealing temperature on growth of Ce-ZnO nanocomposite thin films: X-ray photoelectron spectroscopy study. *Thin solid films*, *520*(2), 721-725.

Zhai, C.-H., Zhang, R.-J., Chen, X., Zheng, Y.-X., Wang, S.-Y., Liu, J., Dai, N., & Chen, L.-Y. (2016). Effects of Al doping on the properties of ZnO thin films deposited by atomic layer deposition. *Nanoscale research letters*, *11*(1), 407.

Zhang, C., Chen, X.-l., Geng, X.-h., Tian, C.-s., Huang, Q., Zhao, Y., & Zhang, X.-d. (2013). Temperature-dependent growth and properties of W-doped ZnO thin films deposited by reactive magnetron sputtering. *Applied surface science*, *274*, 371-377.

Zhang, H., Liu, H., Lei, C., Yuan, C., & Zhou, A. (2010). Tungsten-doped ZnO transparent conducting films deposited by direct current magnetron sputtering. *Vacuum*, *85*(2), 184-186.

Zsigmondy, R., & Scherrer, P. (1912). Bestimmung der inneren Struktur und der Größe von Kolloidteilchen mittels Röntgenstrahlen. *Kolloidchemie Ein Lehrbuch*, *1918*, 387-409.